Live imaging defines the dynamics and molecular basis of *in vivo* mitophagy

Paul J. Wrighton[1], Arkadi Shwartz[1], Jin-Mi Heo[2], Eleanor D. Quenzer[1], Kyle A. LaBella[1], J. Wade Harper[2], Wolfram Goessling[1,3,4,5,6,7,8,*]

[1]Division of Genetics, Brigham and Women's Hospital, Harvard Medical School, Boston, MA 02115, USA.

[2]Department of Cell Biology, Harvard Medical School, Boston, MA 02115, USA.

[3]Harvard Stem Cell Institute, Cambridge, MA 02138, USA.

[4]Dana-Farber Cancer Institute, Harvard Medical School, Boston, MA 02115, USA.

[5]Broad Institute of MIT and Harvard, Cambridge, MA 02142, USA.

[6]Harvard-MIT Division of Health Sciences and Technology, Boston, MA 02115, USA.

[7]Division of Gastroenterology, Massachusetts General Hospital, Harvard Medical School, Boston, MA 02114, USA.

[8]Lead Contact

*Correspondence: wgoessling@mgh.harvard.edu

SIGNIFICANCE

Damaged mitochondria lead to cellular injury and possible apoptosis. Mitophagy is the quality control mechanism to recycle damaged mitochondria. Disrupted mitophagy contributes to aging and other diseases, and therefore elucidation of this process has important health implications. The mechanisms governing mitophagy, however, were discovered predominantly by treating cells *in vitro* with mitochondrial poisons, which may not reflect physiological stress responses occurring *in vivo*. Here, we utilize confocal imaging and mitophagy reporter zebrafish to discover the dynamics of mitophagy and employ genetic epistasis analysis to interrogate the relevance of mitophagy receptors during physiological stresses. Our *in vivo* results elucidate the mitophagy process in a living vertebrate and determine the necessity of specific mitophagy receptor genes for a physiological mitophagy response.

ABSTRACT

Mitophagy defects are linked to aging, sarcopenia, and neurodegenerative diseases. To target this process for clinical intervention, the *in vivo* mitophagy dynamics and molecular mechanisms under physiologically relevant stresses must be better understood. Here, we characterized newly generated mitophagy reporter zebrafish and discovered high basal mitophagy rates in many organs during embryonic development and organogenesis. Rapid time-lapse imaging revealed *in vivo* dynamics of fasting-induced mitophagy, which occur via a piecemeal process. Baseline and stress-induced mitophagy were precisely assessed through ratiometric and volumetric image quantification algorithms. Activation of Hypoxia-inducible factor through physiological stress or chemical or genetic modulation provoked *bnip3*-dependent mitophagy in muscle independent of *pink1*. Surprisingly, disruption of *bnip3la* (*nix*) or *fundc1*, putative hypoxia-associated mitophagy receptors, had no effect on mitophagy. Our results discover fundamental mitophagy dynamics and molecular mechanisms with important implications for mitochondrial quality control and highlight the importance of live imaging *in vivo* studies.

KEYWORDS

Autophagy, Hypoxia, Fasting, Mitochondria, Lysosome

Mitophagy, the removal of damaged mitochondria via autophagy, prevents cellular damage and apoptosis (1). Disruptions in mitophagy are linked to muscular dysfunction (2), neurodegenerative diseases such as Parkinson's Disease and Alzheimer's (3), and drug-induced liver injury (4). Mitophagy also occurs at a basal level in cells with high metabolic rates (5). The extent, functions, and mechanisms involved in basal mitophagy, however, are unclear, especially during embryonic development. Further, the fundamental dynamics and the associated molecular mechanisms of stress-induced mitophagy have primarily been investigated in *in vitro* cell culture. Thus, additional *in vivo* studies are needed to provide novel mechanistic insight.

The kinetics and dynamics of the actual process of mitophagy *in vivo* are unexplored. There are multiple mechanisms observed *in vitro* by which a mitochondrion is sequestered by the autophagy machinery. In the "wholesale" mode, after a mitochondrial filament reaches a damage threshold, membrane depolarization and extensive fragmentation occurs, which is followed by recruitment of the autophagy machinery to degrade the fragments. In the "piecemeal" mode, the damaged part of a mitochondria is sequestered, and the autophagy machinery is localized to that point, which undergoes fission, leaving the filament largely intact—mitophagy occurs piece-by-piece (1, 6, 7). Further, the dynamics of how lysosome and mitolysosome size or number changes in response to increasing mitophagic demand are unknown *in vivo*. These mitophagy modes have not been verified in any live organism or stress context, highlighting the need for precise *in vivo* observations.

Most molecular mechanisms governing mitophagy were initially described *in vitro*, using cell lines often overexpressing PARKIN and non-physiological stresses such as drug exposures to induce widespread mitochondrial membrane depolarization. Thus, it is now vital to use *in vivo* models to validate and contextualize how mitophagy occurs in the multicellular, multi-organ context of an entire organism under physiological conditions. Nutrient deprivation and hypoxia are physiological stresses that induce mitophagy in various contexts. Hypoxia-induced cell

damage can induce mitophagy in mouse embryonic fibroblasts (MEFs) (8) as well as murine liver (9) and muscle (8). In addition, Bnip3-Fox03 signaling is linked to fasting-induced macroautophagy in muscle (10), although hypoxia-induced mitophagy has not been examined. The PINK1-PARKIN pathway governs mitochondrial depolarization-induced mitophagy (11, 12), however, its role in hypoxia-induced mitophagy remains controversial with evidence in other model organisms both for (13, 14) and against (15) a role. Thus,higher order *in vivo* models are necessary to dissect mitophagy mechanisms using genetic epistasis approaches.

Recently, mitochondria-targeted, pH-sensitive fluorescent protein constructs—mito-mKeima (16) (mito-Keima) and mito-EGFP-mCherry (17) (mito-GR; Green Red)—have been developed as sensitive readouts of mitophagy. pH sensitivity of the fluorophores allows for discrimination between healthy mitochondria at neutral pH and mitochondria undergoing degradation in low-pH autolysosomes. Keima and mCherry are resistant to lysosomal degradation allowing for accumulation of the signal, which is interpreted as an integration of the extent of mitophagic flux over time. These biosensors have been incorporated into cell culture models as well as model organisms (5, 9, 15). How long these reporters persist *in vivo* is unknown and, therefore, a major hindrance to the interpretation of data. Murine tissues are also difficult to image live *in situ*, and longitudinal imaging is not practical. *Drosophila* and *C. elegans* are genetically distant from humans, not offering the possibility to examine conserved organ-based processes. Zebrafish are transparent vertebrates that develop completely externally and demonstrate a high degree of conservation to mammalian tissue organization, organ development and molecular signaling (18), complementing the advantages of other models and offering the unique ability to illuminate *in vivo* mitophagy trafficking and subcellular dynamics.

Our work utilizes pH-dependent fluorescent constructs and the zebrafish model to define novel insights into mitochondrial dynamics during vertebrate organ development and physiological stress. We discover widespread basal mitophagy in many organs systems during

development. We illuminate mitophagy dynamics *in vivo*, using time-lapse imaging to observe piecemeal mitophagy and mitolysosomal fission occurring in fasted muscle. For the first time, we measure the *in vivo* off-rate of mito-Keima and determine that it persists as a signal for mitophagy events that occurred in the past 5-7 days. Importantly, using chemical and genetic perturbations, we demonstrate that *bnip3* is necessary for hypoxia-induced mitophagy in muscle independent of *pink1*. With the data presented, we establish fundamental dynamics of *in vivo* mitophagy, define the *in vivo* parameters of these powerful biosensors, and elucidate the genetic and molecular mechanisms governing hypoxia-induced mitophagy.

RESULTS

Transparent larvae reveal widespread mitophagy during organogenesis

We used *tol2*-mediated transgenesis (19) to generate zebrafish lines *Tg(ubi:mito-Keima)* and *Tg(ubi:mito-GR)*, expressing mitochondrial matrix-targeted mito-Keima or mito-GR under the control of the ubiquitin promoter, which is highly expressed in most tissues (20). The ratios of either 561 nm-excitation Keima (acidic: Keima561) signal to 440 nm-excitation Keima (neutral: Keima440) signal or pH-insensitive mCherry signal to the pH-sensitive EGFP signal can differentiate between neutral and acidic conditions. Healthy mitochondria maintain a neutral pH 8 matrix and are labeled with either Keima440 or both EGFP and mCherry. However, mitochondria undergoing degradation will exist in an acidic environment and will be labeled with Keima561 for mito-Keima or mCherry alone for mito-GR.

Ubi:mito-Keima and ubi:mito-GR transgenic zebrafish demonstrated no physiological abnormalities to suggest fluorophore toxicity and were generally analyzed as larvae from 1 to 8 days post fertilization (dpf). To test whether the ubi:mito-Keima construct faithfully reports mitophagy *in vivo*, we exposed ubi:mito-Keima larvae to MitoTracker dye and found that in skin cells, which readily absorbed the dye, both the Keima440 signal and the Keima561 signal colocalized with MitoTracker puncta (Fig. S1*A*). Thus, mito-Keima is correctly localized to

mitochondria. Then, larvae were exposed to lysotracker dye, which accumulates in low-pH organelles, particularly lysosomes. In skeletal muscle cells, Lysotracker colocalized with Keima561 signal, but not with Keima440 signal (Fig. S1*B*). Thus, the Keima561 signal represents mitochondrial remnants that have been trafficked to lysosomes (mitolysosomes). To verify that this process was bona fide mitophagy involving the autophagy machinery, we crossed ubi:mito-Keima fish with *Tg(CMV:EGFP-Lc3)* fish (21), which label autophagosomes and autolysosomes with EGFP. In skeletal muscle, Keima561 puncta colocalized with the EGFP-Lc3 signal, whereas there was no colocalization with Keima440 signal, indicating that to induce degradation, mitochondrial fragments are shuttled to low-pH autolysosomes (Fig. S1*C*). Similarly, we incubated ubi:mito-GR embryos with LysoTracker deep red and observed colocalization with mCherry^{+};GFP^{-} puncta (Fig. S1*D*). Thus, the signals from both reporter lines can clearly differentiate between healthy mitochondria and those undergoing mitophagy.

Next, we utilized the mito-GR line to delineate basal levels of mitophagy during zebrafish development. We observed basal mitophagy in several larval zebrafish tissues. Neural tissues including the hindbrain, olfactory placode, trigeminal ganglion, retina, spinal cord, and neuromasts had high levels of basal mitophagy. The developing notochord, vasculature, heart (ventricle), kidney, and liver all displayed high levels of basal mitophagy, and the pancreas displays moderate levels (Fig. 1*A*). In skeletal muscle—a highly metabolic tissue—before 120 hours post fertilization (hpf), we observed extremely low basal mitophagy (Fig. 1*B*). Zebrafish larvae subsist on nutrients derived from their yolk sac for approximately the first 4.5 dpf. Once yolk sac nutrients are depleted, larvae must transition to external food sources, or they begin to starve. In fish 96 hpf and younger, we observe very low levels of mitophagy in skeletal muscle, but after 120 hpf without external food sources, we observe obvious mitophagy (Fig. 1*B*, arrows). These results reveal widespread basal mitophagy levels throughout larval zebrafish and identify skeletal muscle as a uniquely suited tissue to investigate stress-induced mitophagy mechanisms *in vivo*.

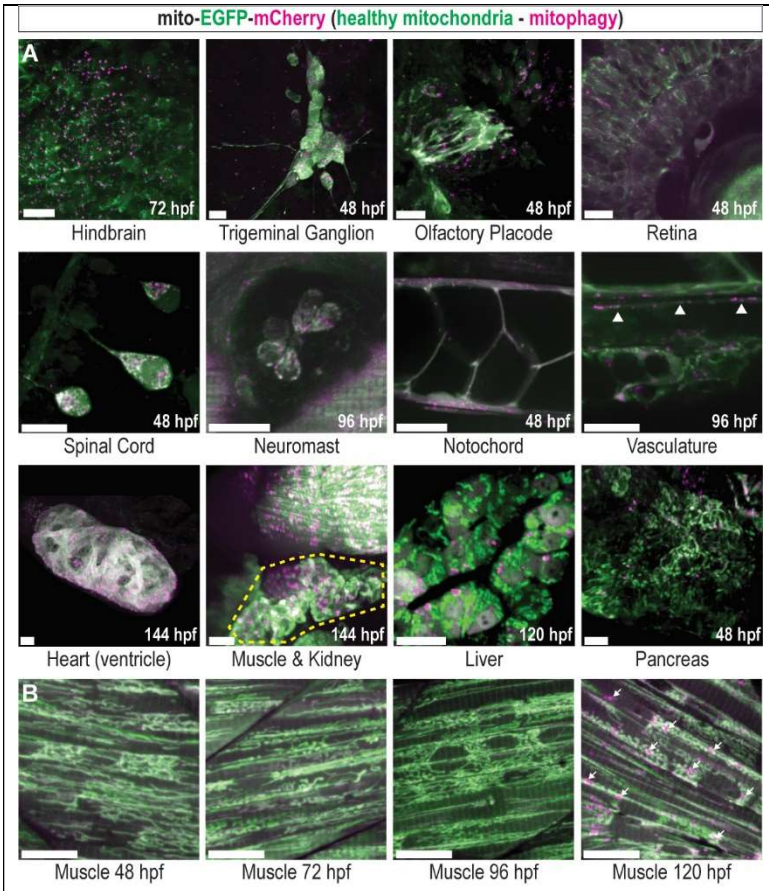

Fig. 1. Basal mitophagy is widespread in developing zebrafish tissues. (*A*) Confocal maximum intensity projection images of mito-GR zebrafish larvae at the indicated developmental time points, displaying various developing organs and tissues. Green indicates EGFP^{high} mitochondria, which are healthy, and magenta indicates mCherry^{high} puncta, representing mitophagy. White arrowheads show vasculature mitophagy. Yellow outline highlights the developing kidney. (*B*) Developmental time series of mito-GR skeletal muscle in the tail. Mitophagy is low at 48, 72 and 96 hpf and high at 120 hpf (arrows). All images are of live ubi:mito-GR larvae except the liver image, which is from fabp10a:mito-GR and the heart image, which is a fixed whole-mount ubi:mito-GR larva. Scale bars, 15 μm.

Fasting induces quantifiable mitophagy and reveals mitolysosome volume dynamics

Skeletal muscle is a mitochondria-rich, highly metabolic tissue, which responds to nutrient deprivation by inducing autophagy (10), but there is limited knowledge about the regulation and dynamics of muscle mitophagy *in vivo*. Fasted 6 dpf larvae exhibited robust

mitophagy. To precisely quantify mitophagy levels, we developed volumetric and ratiometric image analysis methods to rapidly isolate mitophagy puncta from large, 3D tissue volumes and quantify the number and size of the puncta within a tissue (Fig. 2*A*). The Keima561:Keima440 signal ratio isolates mitophagy puncta, the density and volume of which can be measured by applying an isosurface rendering algorithm and normalizing to total tissue volume (Fig. 2*B*). This method is applicable to both ubi:mito-Keima and ubi:mito-GR. However, at greater imaging depths we found ubi:mito-Keima signal decayed more consistently and provided higher signal-to-noise. Thus, we applied this method to quantify fasting-induced mitophagy in ubi:mito-Keima zebrafish in two modes: mitolysosome density, defined as the number of mitophagy puncta per tissue volume, and mitophagy index, defined as the total volume of mitophagy puncta per total tissue volume.

Quantifiable mitophagy in both fed and fasted zebrafish muscle was observed at 5 dpf (Fig. 2c), corresponding with the larval transition from yolk nutrients to external feeding. At this time point, there was no significant difference between fed and fasted zebrafish skeletal muscle in mitophagy puncta density (Fig. 2*D*) or mitophagy index (Fig. 2*E*). Mitophagy index was a more sensitive readout for mitophagy. Mitolysosome density was not significantly altered until after 7 dpf, whereas mitophagy index revealed significant increases by 6 dpf with much larger fold changes. Thus, mitophagy in skeletal muscle occurs after yolk depletion, but is abrogated by feeding.

To understand mitolysosome size dynamics, we examined the volume distribution of individual mitolysosomes enabled by our volumetric image analysis method. In fasted skeletal muscle, the early response from 5 to 7 dpf increased the volume of mitolysosomes—both fed and fasted fish had a monomodal mitolysosome volume distribution with the fasted fish displaying an increase in 25th percentile, 50th, and 75th percentile mitophagy puncta volume (Fig. 2*F* and Fig. S2). However, by 8 dpf, when fasting entered a more advanced stage, the mitolysosome size

distribution became bimodal, with an increase in both large and small mitolysosomes (Fig. 2*F* and Fig. S2). Surprisingly, this result is unique to mitolysosome dynamics: although the size distribution of all lysosomes showed that the average lysosome increased in size and the number of lysosomes increased in fasted larvae over time, very small lysosomes were present at all stages (Fig. S3). Together, these results reveal that the early fasting-induced mitophagy response primarily utilizes existing autolysosomes within the cell as evident by an increase in mitophagy index and shift in the size distribution before significant changes in the mitolysosome density. However, during advanced stages, there is a concomitant increase in both the size and number of mitolysosomes where the existing structures become quite large and new, very small mitolysosomes are observed with an increase in both mitolysosome density and mitophagy index accompanied by a bimodal mitolysosome volume distribution. Taken together, these data validate the developed image quantification methods and reveal the mitolysosome size dynamics as a response to progressing nutrient deprivation.

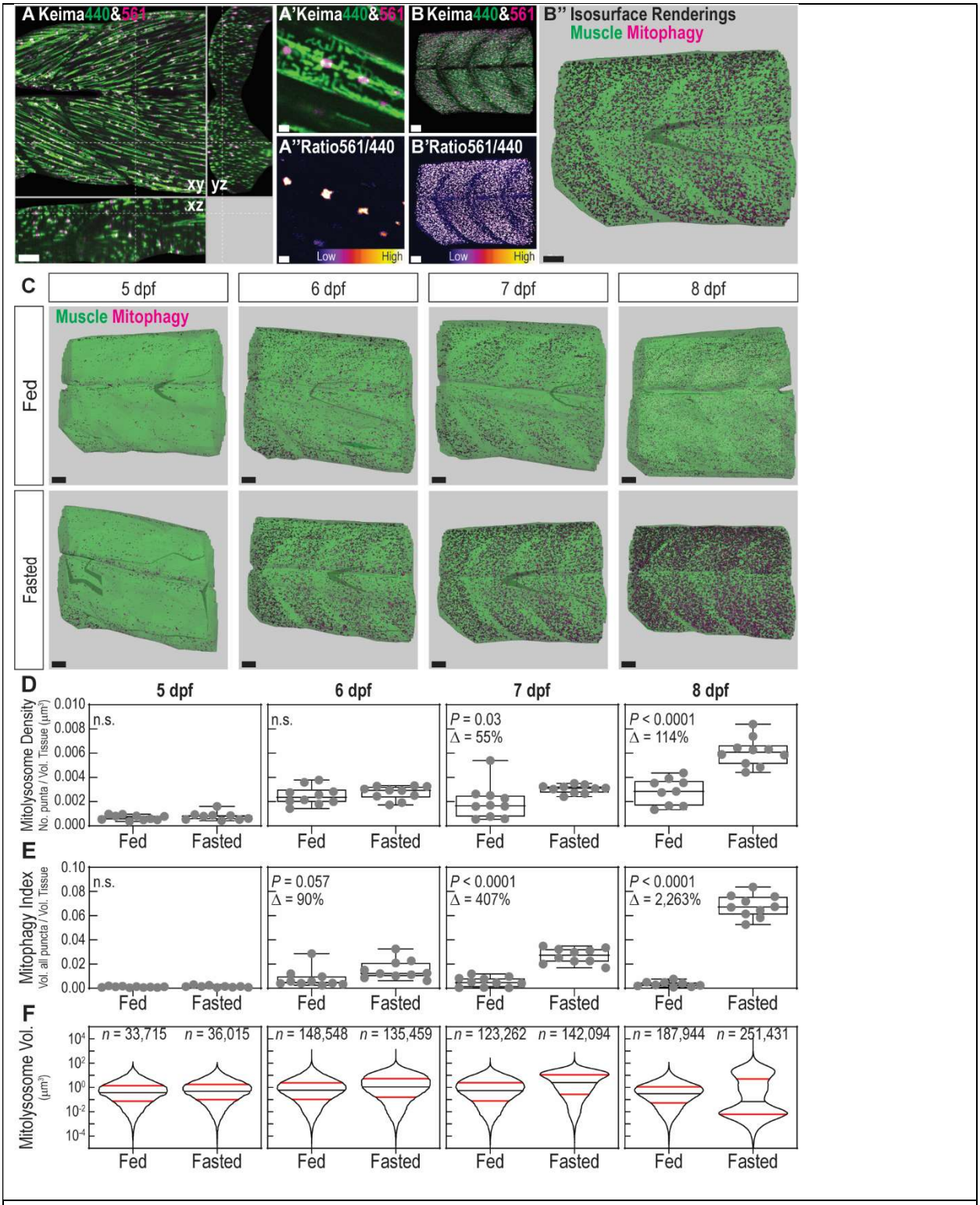

Fig. 2. Volumetric imaging reveals dynamics of fasting induced mitophagy. (*A*) Confocal microscopy cross-sectional image of 6 dpf ubi:mito-Keima zebrafish skeletal muscle demonstrates the typical imaging volume achieved for analyses. Scale, 100 μm. (*A'*) Zoomed image demonstrates mitochondrial resolution achieved for all images and

(*A''*) ratiometric images used to isolate mitophagy puncta. Scale, 3 μm. (*B*,*B'*,*B''*) Representation of the image analysis process. Scale, 30 μm. (*B*) 3D reconstruction of the large volume image showing Keima440 and Keima561 signal throughout greater than 6 myotomes. (*B'*) Ratiometric image isolates Keima561^{high} mitophagy puncta. (*B'')* Isosurface renderings of muscle tissue volume (green) and the mitophagy puncta (magenta) allow for volumetric analysis of mitophagy. (*C*) Isosurface renderings of muscle volume and mitophagy puncta in 5-8 dpf zebrafish either fed or fasted. Green is the surface rendering of the muscle tissue, and magenta are surface renderings for individual mitophagy puncta. Scale, 30 μm. (*D*) Quantification of Mitolysosome Density defined as the number of mitophagy puncta divided by the total tissue volume. Data shown are median, 1st and 3rd quartiles, minimum and maximum. *P*, unpaired, two-tailed Student's t test. n.s., not significant (P>0.05). Δ, percentage change of experimental cohort to control cohort. (*E*) Quantification of Mitophagy Index defined as the sum of the volumes of all mitophagy puncta divided by the total tissue volume. Data shown are median, 1st and 3rd quartiles, minimum and maximum. *P*, unpaired, two-tailed Student's t test. n.s., not significant (P>0.05). Δ, percentage change of experimental cohort to control cohort. (*A*-*E*) Each dot represents one larva. (*F*) Violin plots demonstrating the volume (μm^3) distribution of individual mitolysosome puncta from all the fed or fasted zebrafish in each cohort. Significant changes in the size distributions are evident at every time point (see Supplementary Fig. 2). Data shown are 50th percentile as a black line 25th and 75th percentiles as red lines. *n*, number of individual mitolysosomes combined from all larvae.

Mitophagy and mitolysosome fission are rapid

To directly observe the *in vivo* dynamics of mitophagy and mitolysosomes we performed a time-lapse analysis on a 7 dpf fasted mito-Keima larva. We continuously acquired images, finishing each imaging volume approximately once per second and tracking skeletal muscle mitochondria in an approximately 2 cell-deep volume for 28 s (Fig. 3 and Movie S1). To track the movement and dynamics of mitochondria and mitophagy puncta, we generated ratiometric images and isosurface masks (Fig. 3*A*) and applied an object tracking algorithm. To determine the source of the newly appearing, small mitophagy puncta during prolonged fasting, we used the tracking algorithm to identify *de novo* mitophagy events as well as mitolysosome fission events. We binned each event into one of several categories. If the mitophagy punctum stemmed from a healthy, neutral pH mitochondrion, it was considered "new mitophagy". If the punctum broke

away from a different, larger mitophagy punctum, it was considered a “split mitolysosome”. If the punctum migrated into the imaging volume near the edges, it was considered “from outside”. Out of 381 objects, 325 were stable throughout the image, 11 migrated from outside, only 3 were new mitophagy (Fig. 3*C*, * and yellow surface object), and 37 puncta split from larger autolysosomes (Fig. 3*D*, *). Thus, *de novo* mitophagy is rapidly occurring during this stage of fasting and accounts for some of the new small mitolysosomes, but mitolysosome fission is the predominant source of the small mitolysosomes.

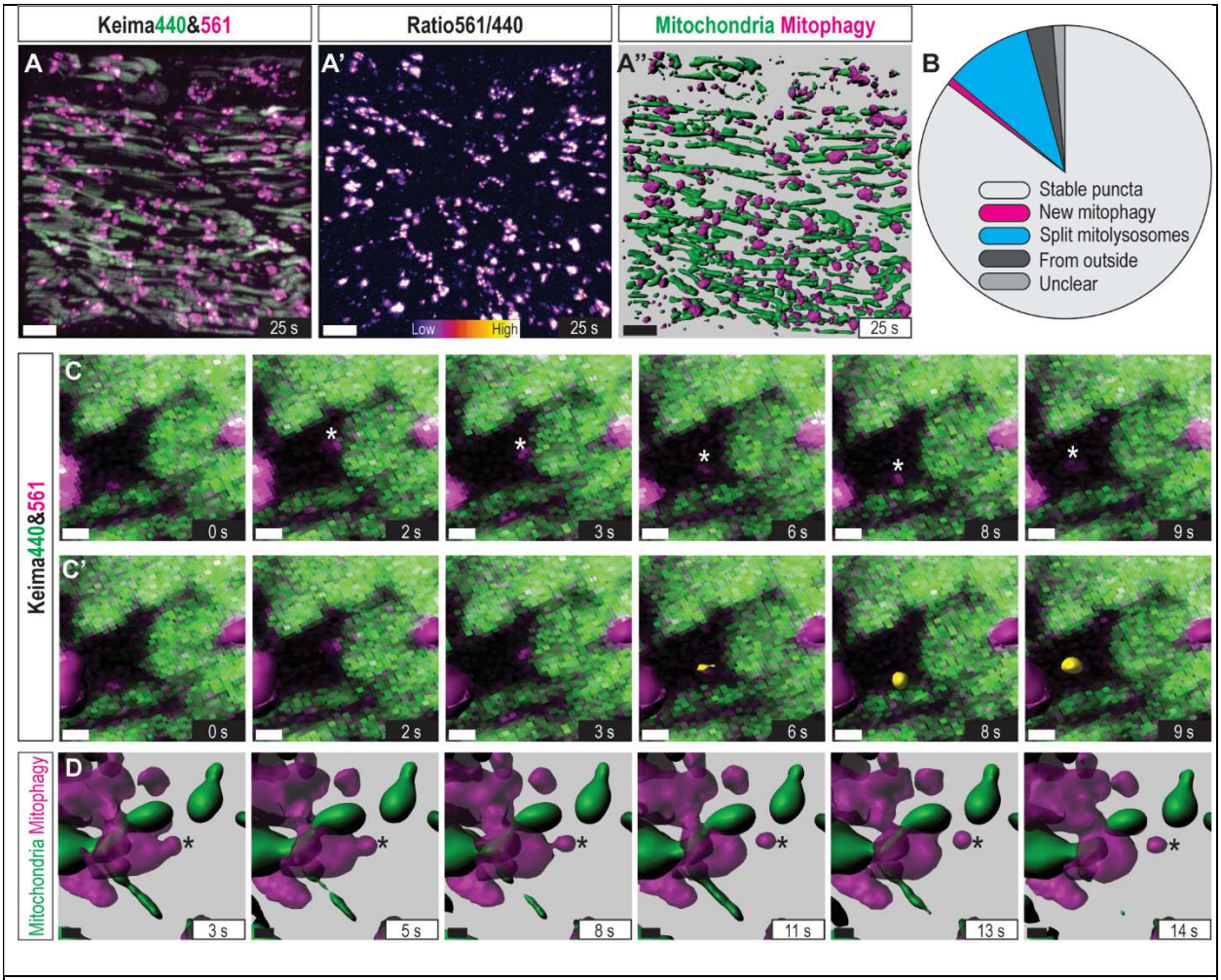

Fig. 3. *In vivo* mitophagy dynamics: mitophagy kinetics and mitolysosome fission. (*A*) Confocal 3D projection of the imaging volume in Movie 1. Images of skeletal muscle in a 7 dpf larva during advanced nutrient deprivation. (*A'*) Ratiometric image isolating areas of mitophagy. (*A''*) Isosurface rendering of mitochondria (green) and mitophagy puncta (magenta) used to track mitochondria, mitophagy, and mitolysosome fission. Scale, 10 μm. (*B*) Classification

of each mitophagy puncta revealing that approximately 85% of mitophagy puncta tracks are stable, 1% of mitophagy puncta are newly formed, and 10% have split from existing, larger mitolysosomes within the 28 s. The remaining mitophagy puncta are pre-existing or translocated from outside the imaging volume. (*C*) Zoomed timeseries of a representative "new mitophagy" event marked with (*). (*C'*) Same as (*C*) with isosurface objects for stable mitophagy puncta (magenta) and the new mitophagy punctum (yellow). Scale, 1 μm. (*D*) Isosurface representation of a splitting mitolysosome (*). Scale, 1 μm.

Mitophagy occurs piece-by-piece

To further define the real time dynamics of mitophagy *in vivo*, we performed time-lapse imaging on 6 dpf fasted *Tg(CMV:GFP-Lc3)*^{zf155};(*ubi:mito-Keima)* zebrafish skeletal muscle. Over the course of 25 minutes (in 5-minute intervals), a GFP-Lc3^{+} autophagosome sequestered a portion of a filamentous mitochondrion, and the fluorescence spectrum of Keima shifted from the 440 nm excitation to the 561 nm excitation indicating pH change. Then, the small autolysosome containing the newly engulfed mitochondrion (Fig. 4*A*, arrow) translocated and fused with an existing, much larger automitolysosome (Fig. 4*A*, * and Movie S2). This is the first intravital time-lapse mitophagy analysis tracking mitochondrial fission, pH change, and trafficking to autolysosomes in a vertebrate, and it raises interesting questions regarding the mechanics of mitophagy.

It is unknown whether *in vivo* mitophagy occurs via the wholesale or piecemeal mode. To probe how GFP-Lc3 structures interact with mitochondria *in vivo*, we performed an additional time-lapse analysis in ubi:mito-Keima;GFP-Lc3 larvae with greater time resolution, and observed several interesting phenomena. We observed the GFP-Lc3 signal extend thin processes throughout the cell. In one instance, thin processes emerged from an Lc3^{+} structure, tracing the surface a large mitochondrion but quickly retracted (Fig. 4*B*, arrow and Movie S3). To better visualize and track mitochondrial quality control process, we generated isosurface renderings to identify and track the different organelle structures in three dimensions. Mitophagy events

(transition from Keima440^{high} to Keima561^{high}) occurred at discrete points along the filamentous mitochondria, often near the poles. Interestingly, we never observed massive mitochondrial fragmentation followed by mitophagy, indicating the wholesale mode of mitophagy is not active in this context. In contrast, we found mitochondrial fission and mitophagy occurring at discrete contact points between Lc3 and filamentous mitochondria (Fig. 4*C*, arrow and Movie S4), indicative of piecemeal mitophagy. Our results show that during fasting, Lc3^{+} structures extend processes throughout the mitochondrial environment and mitophagy occurs piece-by-piece.

Mitochondrial substructures can also be removed piecemeal by an Lc3-independent mechanism utilizing mitochondria-derived vesicles (MDVs) (22, 23). However, we find nearly complete colocalization of the Keima561 mitophagy signal with GFP-Lc3 signal (Fig. 4 and Movies S2-4). Thus, in fasted muscle, the MDV pathway does not appear to be a major mitochondrial quality control mode activated. In sum, these data support the conclusion that in fasted skeletal muscle, mitophagy occurs primarily by a piecemeal mitochondrial fission mechanism directly into Lc3^{+} structures.

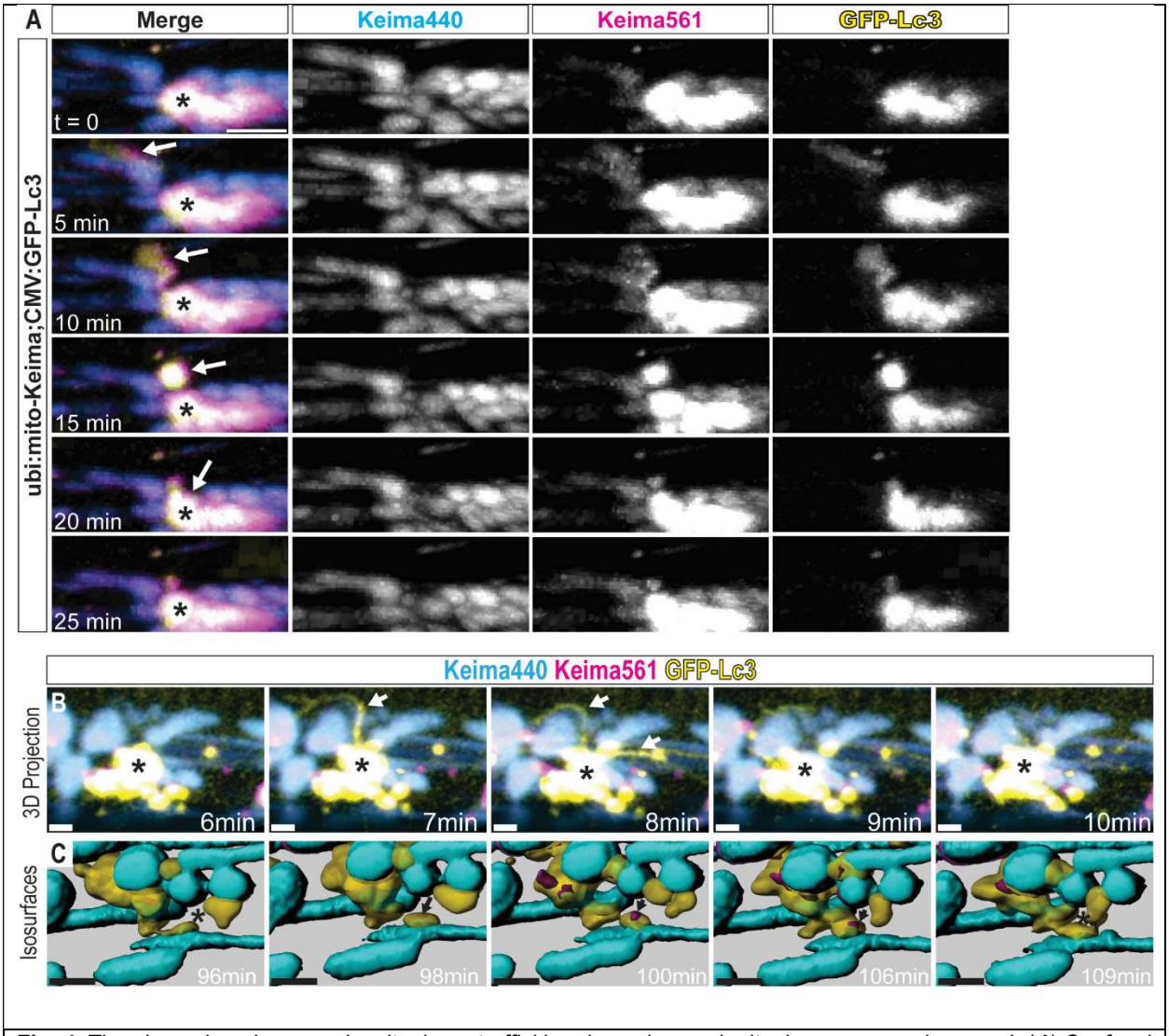

Fig. 4. Time-lapse imaging reveals mitophagy trafficking dynamics, and mitophagy occurs piecemeal. (*A*) Confocal time-lapse imaging of the skeletal muscle in fasted 6 dpf ubi:mito-Keima;GFP-Lc3 zebrafish. At t = 0, several healthy mitochondria (Keima440^{high}) reside near an existing autolysosome containing mitochondrial remnants (*, Keima440^{low};Keima561^{high};Lc3^{+}). At t = 5-10 min, a new Lc3^{+} autolysosome is present (arrow), and it contains part of the previously healthy mitochondrion, which has shifted to Keima561^{high} indicating acidic conditions (arrow). This newly formed automitolysosome then translocates (t = 15 min) and fuses (t = 20-25 min) with the larger, pre-existing automitolysosome (*). (*B*) 3D projections of confocal time-lapse imaging of fasted skeletal muscle in 5 dpf ubi:mito-Keima larva. A large autolysosome (Lc3^{+} puncta) contains degraded mitochondria (magenta; overlap with yellow appears white; *). Over time, this autolysosome extends projections (7 min and 8 min; white arrows) near the surface of healthy mitochondria (Keima440^{high}). In this case, the protrusion retracts (9 min and 10 min), and no new mitophagy occurs. (*C*) Isosurface renderings of later time points in the same imaging series as (*B*). Mitophagy occurs

piecemeal. An Lc3-positive surface is interacting with a Keima440^{high} filamentous mitochondrion (96 min; *). Then, a small portion of the longer filamentous mitochondrion undergoes fission and becomes Keima561^{high}, indicating pH change (98-106 min; arrow) and detaches (109 min; *).

Keima mitophagy signal persists for days

Keima is resistant to lysosomal degradation, which is a prerequisite for its function as a biosensor (16). It is unknown, however, how long the florescent signal remains as a signal for "mitophagy occurred" either *in vitro* or *in vivo*. To assess this important aspect, we injected wild type (WT) embryos with an inducible mito-Keima construct (hsp70:mito-Keima), generating mosaic animals. The larvae were fasted from 4.5 to 6.5 dpf to induce a pulse of mitophagy, and a pulse of mito-Keima expression was induced by heat shock at 6 dpf. Then, fish were fed to prevent additional mitophagic flux, and we identified suitable cells to track longitudinally from 13-22 dpf (Fig. 5*A* and Fig. S4*A*). We tracked individual cells in two animals where the Keima440 signal was low or non-detectable, indicating that there was low labeling of remaining healthy mitochondria (Fig. 5*B* and Fig. S4*B*). The uniform decrease in the overall Keima signal over time demonstrated that additional Keima protein was not being translated (Fig. 5*B*' and Fig. S4*B'*). Using this unique approach, we tracked a decrease in the number of Keima561 puncta, yielding a measure of the duration Keima remains fluorescent within the autolysosome *in vivo*. The number of Keima561 puncta within a single myotube dropped from 101 to 5 over the course of 7 days (Fig. 5*C*). Similarly, a cell in a different animal showed a drop from 19 to 5 over 4 days (Fig. S4*C*). Because many of the mitolysosomes are immobile, we tracked a single mitophagy punctum, which persisted in each of the 5 daily images (Fig. S4*D*). The Keima signal did not recover after photobleaching, validating that no new Keima protein was being translated (Fig. S4*D*). These results uniquely demonstrate the biological persistence of the mitophagy fluorescent signal and support the conclusion that mito-Keima signal represents the integration of the mitophagic flux

over at least 5-7 days, which should inform the design and interpretation of experiments using mito-Keima reporters *in vivo*.

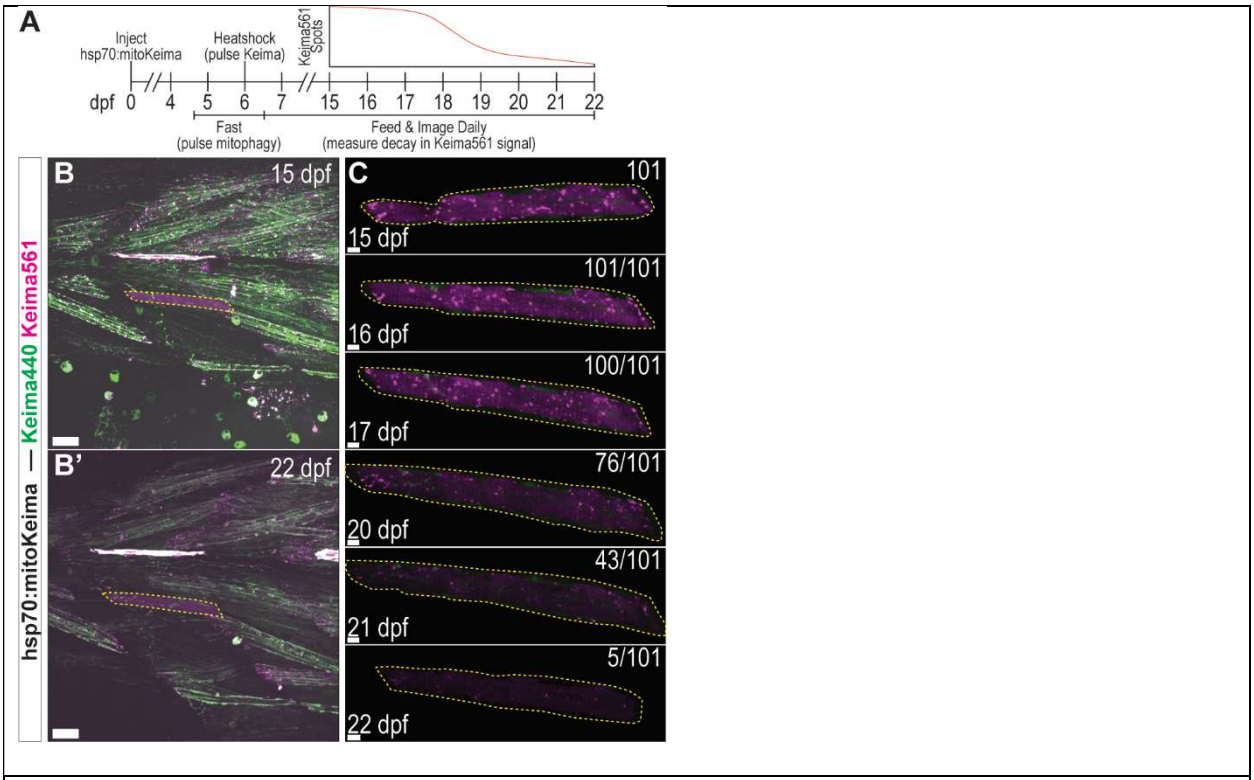

Fig. 5. *In vivo*, mito-Keima signal persists as stable integrative record for 5-7 days. (*A*) Experimental design to induce a pulse of mitophagic flux and longitudinally track Keima561 puncta in an individual cell for days as the signal diminishes. Fish were fasted from 4.5-6.5 dpf to pulse mitophagic flux then fed to minimize any additional mitophagy. Keima was pulsed by heat shock at 6 dpf. (*B*,*B'*) Zoomed out images of a cell (outlined in yellow) tracked from 15 to 22 dpf. This demonstrates the tracking of the single myotube depicted in (*C*). (*B'*) also demonstrates the overall decrease in mito-Keima signal over time showing that no new Keima was translated after the initial pulse. Scale, 30 μm. (*C*) Longitudinal images of a single myotube (outlined in yellow) from 15-22 dpf. The number in the top right corner indicates the number of mitophagy puncta detected within the cell compared to the 15 dpf timepoint, which decreases over the course of 7 days. Scale, 5 μm.

Hif activation induces mitophagy

Tissue hypoxia (ischemia) leads to mitochondrial damage and production of excess reactive oxygen species (24). Therefore, we applied our zebrafish mitophagy reporter system to

hypoxia-induced mitophagy in zebrafish skeletal muscle (Fig. 6*A*). To avoid nutrient deprivation-induced mitophagy as a confounding variable, we focused on larvae younger than 5 dpf (Fig. 1). Zebrafish larvae were raised in hypoxic fish water within a hypoxic chamber (4.7% oxygen) from 77-96 hpf, causing death in 11 of 35 larvae, indicative of the substantial hypoxic stress induced by this approach. The remaining larvae had a significant increase in mitophagy in skeletal muscle (Fig. 6*B*). Varying the percent oxygen or exposure time either caused universal death with larvae displaying opaque brain tissue indicative of necrosis, or less robust increases in mitophagy (data not shown).

Next, we tested whether other activators of hypoxia inducible factor (Hif) signaling could induce mitophagy in skeletal muscle using the PHD inhibitor dimethyloxalylglycine (DMOG, Fig. 6*A*) (25–27). DMOG exposure from 3-4 dpf induced robust mitophagy compared to vehicle controls (Fig. 6*C*). We confirmed this result by exposing zebrafish to FG-4592 (Roxadustat), a chemically dissimilar, PHD inhibitor evaluated for FDA approval, and observed a similar increase in mitophagy in skeletal muscle (Fig. 6*D*). Similarly, knockdown of *vhl*, a negative regulator of Hif, via antisense morpholino (28) induced mitophagy in skeletal muscle at 3 dpf (Fig. 6*E*). To test whether Hif activation alone was sufficient to induce mitophagy in skeletal muscle in a cell autonomous manner, we expressed a dominant active Hif (29) (*DA-hif1ab*) and nuclear-localized EGFP under the control of the muscle-specific *unc45b* promoter (30). This resulted in mosaic expression of nuclear EGFP, which was concomitant with high levels of mitophagy. In contrast, surrounding EGFP^{negative} cells had little to no mitophagy similar to uninjected controls (Fig. 6*F*). These results confirm that zebrafish muscle responds to hypoxia and Hif-activation by inducing mitophagy in a cell autonomous fashion, and further demonstrate the sensitivity and consistency of our analysis method.

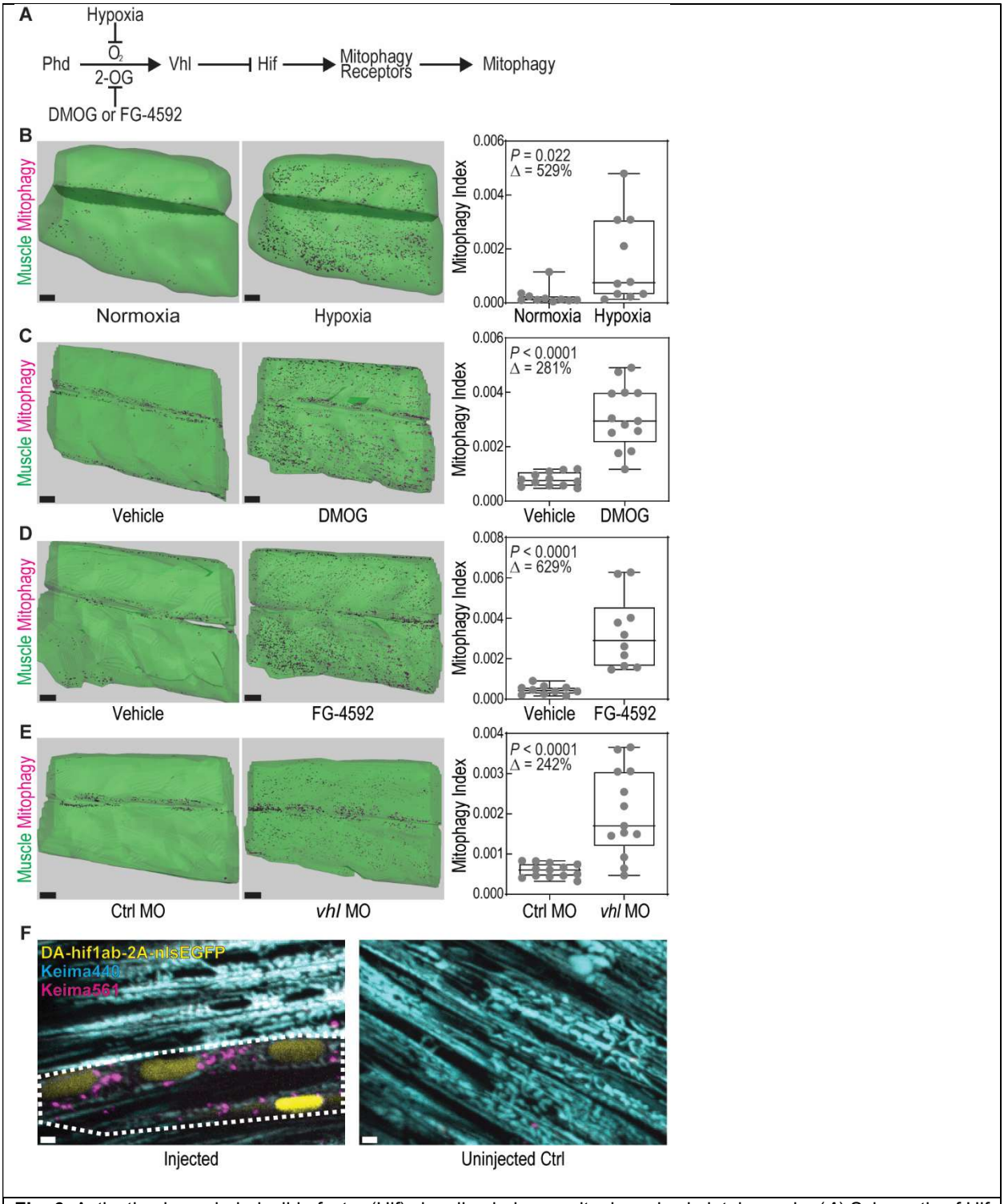

Fig. 6. Activating hypoxia-inducible factor (Hif) signaling induces mitophagy in skeletal muscle. (*A*) Schematic of Hif signaling. 2-OG, 2-oxoglutarate. (*B-E*) Isosurface renderings and mitophagy index quantification in skeletal muscle of 4 dpf ubi:mito-Keima zebrafish exposed to (*B*) 4.7% oxygen (hypoxia) from 3-4 dpf, (*C*) 60 μM DMOG from 3-4

dpf, or (*D*) 10 μM FG-4592 from 3-4 dpf. **e**, Isosurface renderings and quantification of mitophagy in skeletal muscle of 3 dpf zebrafish injected with control (Ctrl) or *vhl* antisense morpholinos (MO). Scale bars, 30 μm. Data shown are median, 1st and 3rd quartiles, minimum and maximum. *P*, unpaired, two-tailed Student's t test. Δ, percentage change of experimental cohort to control cohort. Each dot in every graph represents one larva. (*F*) Confocal microscopy images of 4 dpf ubi:mito-Keima expressing dominant active (DA) *hif1ab* in a mosaic fashion. Keima440 is cyan. Keima561 is magenta. Nuclear EGFP is yellow and indicates the cells that express *DA-hif1ab*. White dotted line outlines two adjacent myotubes expressing *DA-hif1ab* and undergoing mitophagy. Scale bars, 2 μm.

Hif-induced mitophagy requires *bnip3* independent of *pink1*

Next, we used the volumetric *in vivo* mitophagy quantification method to illuminate the molecular mechanisms required for hypoxia-induced mitophagy in vertebrate skeletal muscle. First, we tested whether the mitophagy signal resulting from DMOG treatment was dependent on macroautophagy. Larvae were exposed to DMOG to induce mitophagy, and a cohort was treated with SAR405, which inhibits Vps34, a protein necessary for autophagosome formation (31). Treatment with SAR405 drastically abrogated DMOG-induced mitophagy (Fig. 7*A*). Therefore, macroautophagy is vital for Hif-induced mitophagy.

HIF-induced mitophagy is thought to be independent of the PINK1-PARKIN mitophagy pathway and instead rely on the function of specific proteins such as BNIP3, BNIP3L (NIX), and FUNDC1, which contain LC3-interacting regions (LIRs) (32, 33). Zebrafish are well suited for rapid genetic epistasis analyses using high-efficiency CRISPR mutagenesis in the F0 generation (34). Adapting this method, we tested the necessity of *bnip3*, *bnip3la* (*nix*), and *funcd1* for DMOG-induced mitophagy in vertebrate muscle. Larvae injected with a *bnip3*-targeted CRISPR cutter (CC) showed dramatic reduction in DMOG-induced mitophagy, indicating that loss of *bnip3* function is sufficient to prevent Hif-induced mitophagy in vertebrate skeletal muscle (Fig. 7*B*). Surprisingly, disrupting other Hif-target genes implicated in mitophagy, specifically *bnip3la* (*nix*) (Fig. 7*C*) and *fundc1* (Fig. 7*D*), had no effect on DMOG-induced mitophagy. These results indicate

that *bnip3,* but not *bnip3la* (*nix*) or *fundc1,* is necessary for Hif-induced mitophagy in vertebrate skeletal muscle.

BNIP3 has been shown to interact directly with PINK1, promoting mitophagy via the PARKIN pathway (14), and a study in flies showed pink1 to be necessary for hypoxia-induced mitophagy (13). We found that DMOG exposure increased *bnip3* and *prkn* transcript levels but not *pink1*, *bnip3la* (*nix*), or *fundc1* in whole larvae (Fig. S5*A*). However, there were no significant differences in Hif-induced mitophagy in skeletal muscle between fish homozygous for an established *pink1* null allele (gi2) (35) and their WT or heterozygous siblings (Fig. 7*E*). Larvae injected with an established *pink1* morpholino (36) similarly showed no difference in DMOG-induced mitophagy compared to control-injected siblings (Fig. S5*B*). Furthermore, we used CRISPR to generate an additional *pink1* mutant allele containing a 76 base pair deletion and an early stop codon, which also displayed no differences in DMOG-induced mitophagy compared to siblings (Fig. S5*C*). Likewise, disruption of *prkn* had no effect (Fig. 7*F*). Together, our results support the conclusions that Hif-induced mitophagy in vertebrate skeletal muscle is dependent on *bnip3*, independent of *pink1* and *prkn*, and that *bnip3la* (*nix*) and *fundc1* are not necessary (Fig. 7*G*).

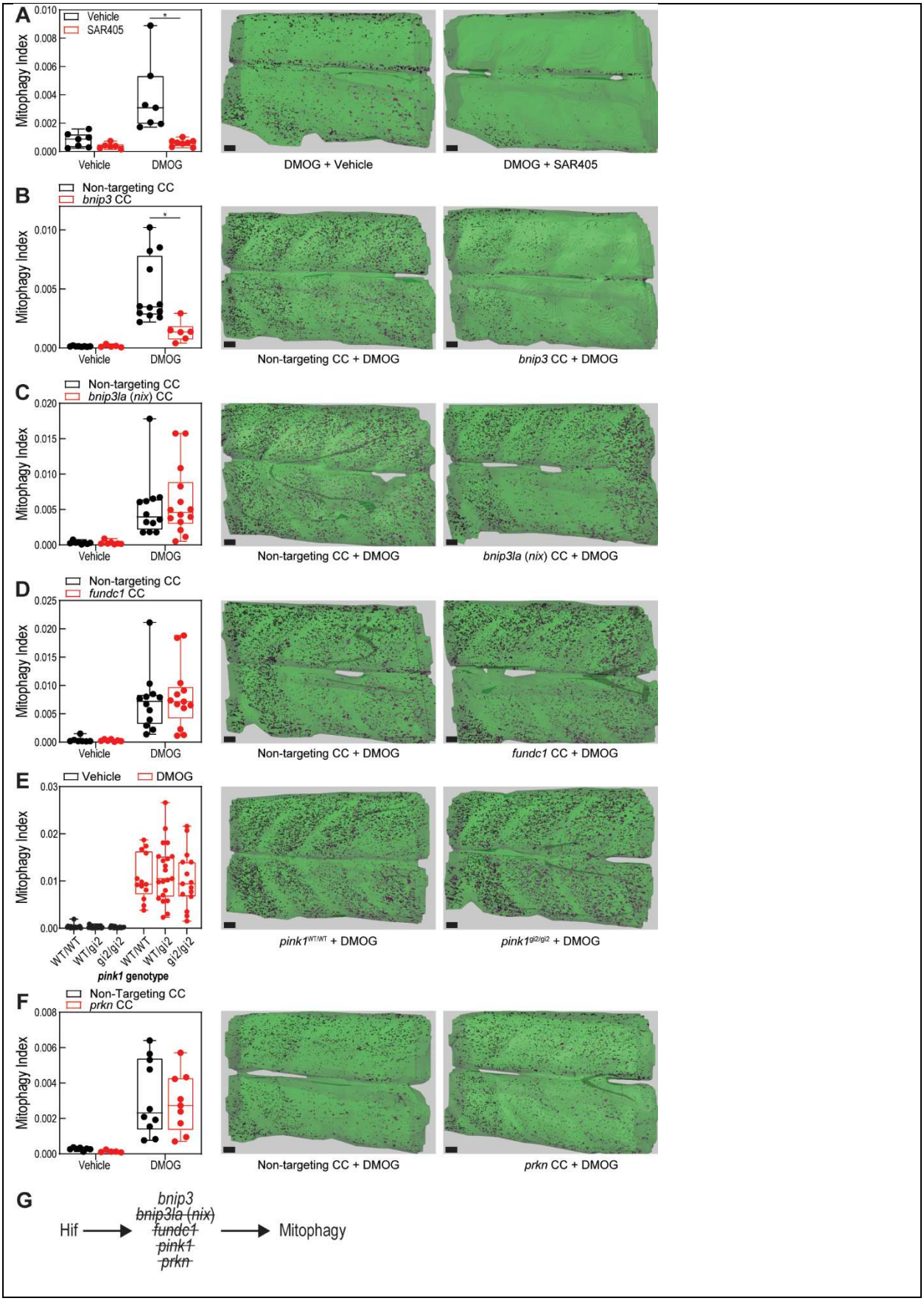
A
Vehicle
SAR405
Mitophagy Index
0.010
0.008
0.006
0.004
0.002
0.000
Vehicle
DMOG
DMOG + Vehicle
DMOG + SAR405
B
Non-targeting CC
bnip3 CC
0.010
0.005
0.000
Non-targeting CC + DMOG
bnip3 CC + DMOG
C
Non-targeting CC
bnip3la (nix) CC
0.020
0.015
0.010
0.005
0.000
bnip3la (nix) CC + DMOG
D
Non-targeting CC
fundc1 CC
0.025
0.020
0.015
0.010
0.005
0.000
fundc1 CC + DMOG
E
Vehicle
DMOG
0.03
0.02
0.01
0.00
WT/WT
WT/gi2
gi2/gi2
pink1 genotype
pink1WT/WT + DMOG
pink1gi2/gi2 + DMOG
F
Non-Targeting CC
prkn CC
0.008
0.006
0.004
0.002
0.000
prkn CC + DMOG
G
Hif
bnip3
bnip3la (nix)
fundc1
pink1
prkn
Mitophagy

Fig. 7. Hif-induced mitophagy requires *bnip3* but not *bnip3la* (*nix*), *fundc1, pink1*, or *prkn*. (*A*) Mitophagy Index quantification of larvae treated with 100 μM DMOG or vehicle (DMSO) and 20 μM SAR405 or vehicle (DMSO). Representative isosurface rendering images show the effect of SAR405 treatment on DMOG-induced mitophagy. (*B-D*,*F*) Mitophagy Index quantification and representative isosurface rendering images of DMOG-induced mitophagy in larvae injected with CRISPR cutters (CC) targeting (*B*) *bnip3*, (*C*) *bnip3la* (*nix*), (*D*) *fundc1*, or (*F*) *prkn*. Scale bars, 20 μm. (*E*) Mitophagy Index quantification and representative isosurface rendering images of DMOG-induced mitophagy in larvae carrying a null *pink1* allele (gi2) and siblings. (*A-F*) Data shown are median, 1st and 3rd quartiles, minimum and maximum. *P<0.01, two-way ANOVA with Holm-Sidak's multiple comparisons test. Each comparison between vehicle- and DMOG-treated samples was also significant (P<0.05) except in (*A*) vehicle controls to DMOG+SAR405 and (*B*) vehicle controls to DMOG + *bnip3* CC. Scale, 20 μm. (*G*) Schematic demonstrating Hif-induced mitophagy requires *bnip3* but not *bnip3l* (*nix*), *fundc1*, *pink1*, or *prkn*. Each dot in every graph represents one larva.

DISCUSSION

In this study, we reveal fundamental characteristics of *in vivo* mitophagy during normal organ development and physiological stress using highly sensitive and specific mitophagy reporter zebrafish combined with precise imaging analysis methods. Basal mitophagy occurs in many developing organ systems. In fasted skeletal muscle, mitolysosomes initially increase in size, followed by a period of concurrent mitophagy and mitolysosome fission. Fasting-induced mitophagy occurs *in vivo* via a piecemeal mechanism. Finally, Hif activation induces mitophagy in skeletal muscle and requires *bnip3* function, but *pink1*, *prkn*, *bnip3la* (*nix*), and *fundc1* are dispensable. In sum, these results reveal *in vivo* cellular and molecular mechanisms regulating physiological-stress induced mitophagy.

A new class of pH-sensitive biosensors is now being used to uncover autophagy mechanisms. Versions of EGFP-mCherry-Lc3 have been incorporated into cells, zebrafish (37), and mice (38) as a quantifiable macroautophagy sensor. Similar pH-sensitive sensors have been adapted to track selective autophagy of mitochondria (17), ribosomes (39), and endoplasmic

reticulum (ER) (40). To effectively employ these autophagy biosensors *in vivo*, however, image capture and analysis protocols must be both rapid and precise. The presented method expands upon previously developed methods to quantify mitophagy from images of mito-Keima and tandem fluorescent protein reporters (5, 9, 16, 41) by combining a ratiometric image set to precisely isolate mitophagy puncta and isosurface-based volumetric analysis to increase fidelity and sensitivity. Capture and analysis of large tissue volumes in whole-mounted live larvae minimizes the sampling bias inherent in other imaging based-quantification methods and therefore represents a substantial improvement over typical confocal microscopy-based methods, which generally quantify only few cells and/or a very thin axial slice, such as a cryosection. Importantly, we demonstrate that the volumetric quantification method we developed is vastly more sensitive to detecting changes in mitophagy levels than methods based on the number of low pH puncta, which have also been used to quantify mitophagy (15, 42).

Transgenic animals expressing pH-sensitive mitophagy reporter constructs have begun to reveal basal mitophagy levels *in vivo*. Studies in mice demonstrated that adult tissues with high metabolic demands—brain, liver, kidney, spleen, skeletal muscle have high basal mitophagy levels (5, 9). Similarly, studies in flies show basal mitophagy in the central nervous system, epidermis, and muscle (15). Our study is the first to detect widespread mitophagy in larval zebrafish during the development of many organs, including several previously unrecognized, such as the spinal cord, notochord, vasculature, pancreas and liver. The developing mouse heart and kidney display high mitophagy, but extensive developmental analysis has not been performed (5). While we and others have revealed the wide extent of basal mitophagy during both development and adult homeostasis, the importance of and regulatory mechanisms governing basal mitophagy are unknown. For instance, Pink1 is not needed for basal mitophagy (15, 38). Disruption of macroautophagy via AMBRA1 mutation causes developmental defects in mice (43) and zebrafish (44), but this is not specific to mitochondria. Nix-mediated mitophagy is vital for differentiation

and maturation of specific cell types such as erythrocytes (45, 46) and retinal ganglion cells (47), but other highly mitophagic tissues are unaffected by Nix depletion. Recently, *nipsnap1* mutant zebrafish were found to have decreased basal mitophagy in skin and defects in dopamine neuron development (42). Thus, zebrafish mitophagy reporters facilitate the discovery of cellular, molecular, genetic and organism-wide developmental mitophagy mechanisms.

The *in vivo* dynamics of mitophagy have not been studied with high precision. Using rapid, continuous acquisition time-lapse imaging, we precisely detected both mitophagy and mitolysosomal fission, generating large and small mitolysosomes during fasting. We observed $Lc3^+$ autolysosomes dynamically extending processes throughout the cell—perhaps recruited to "eat me" signals. These $Lc3^+$ autolysosomes interacted with mitochondrial filaments at distinct points often near the termini, and mitophagy occurs at those locations. Our *in vivo* results fit well with a recent report demonstrating that mitochondrial division occurs concurrently with autophagosome formation in yeast and HeLa cells (6). It will be important to determine why mitophagy occurs at specific mitochondrial locations *in vivo*. A recent study implicates the topology and shape of mitochondria as a driving force for starvation-induced mitophagy in osteosarcoma cells (48). Differential segregation and phosphorylation of mitochondrial matrix proteins was also shown to determine mitophagy rates of different mitochondrial proteins (49, 50). It is exciting to speculate that different mitochondrial proteins could segregate to specific subdomains and dictate the location of mitochondrial fission and mitophagy.

There are two observed mechanisms by which mitophagy occurs *in vitro*: the wholesale mechanism, where a mitochondrial filament reaches a threshold of damage, extensive fragmentation occurs, followed by Lc3 recruitment and fragment degradation, versus the piecemeal mechanism, where a mitochondrial filament becomes damaged, sequesters the damaged components, Lc3 is recruited locally, followed by fission and mitophagy of only that subdomain (1, 7, 51, 52). Our results demonstrate that *in vivo* mitophagy occurs piecemeal in

fasted skeletal muscle. Lc3^{+} structures localize adjacent to discrete points on filamentous mitochondria, fission occurs, and a new Keima561^{+} mitochondrial fragment is sequestered inside the Lc3^{+} organelle. This stepwise nature of mitophagy in skeletal muscle may be an adaptation necessary to allow for muscle mitochondria to exist as large, fused networks, which more efficiently generate ATP and other metabolites (53, 54). Indeed in mice, skeletal muscle-specific deletion of Opa1, a protein necessary for inner mitochondrial membrane fusion, leads to fragmented mitochondria in muscle, muscle degradation, mitochondrial dysfunction, and mitophagy defects (55).

Different types of piecemeal mitophagy have been discovered. The evidence for turnover of mitochondrial components occurring piecemeal has focused on PINK1-PARKIN-mediated mitophagy (7, 51) rather than fasting-induced mitophagy, which is PINK1-PARKIN-independent. Interestingly, an LIR-containing protein TEX264 was recently demonstrated to be necessary for piecemeal selective autophagy of the ER in HEK293 cells (49), proving that receptor-mediated selective autophagy can also occur piecemeal. In Hela cells, a homeostatic piecemeal mitophagy mechanism relies on p62 and LC3C but not PINK1-PARKIN to regulate oxidative phosphorylation (52). A recent study explored mitophagy kinetics using mild oxidative stress to induce more physiological levels of mitophagy in cultured rat neurons indicating that perhaps mild mitochondrial stresses better model the *in vivo* process (56). It is possible the wholesale mechanism only occurs during autophagic cell death or is primarily an *in vitro* artifact caused by artificially high mitochondrial stress levels. It will be important for future work to analyze the mitophagy trafficking dynamics and mechanisms *in vivo* in other cells types and under different physiological stresses to uncover endogenous mitophagy kinetics and to determine if every instance of mitophagy occurs via a piecemeal mechanism.

An important aspect of Keima's biosensor function is its resistance to degradation. Signal survives at least 6 h in the lysosomes of cultured cells (16), but maximum survival time *in vitro* or

in vivo has previously not been measured. Using longitudinal imaging, we measured the Keima off-rate in muscle and showed that Keima signal persists for at least 5-7 days *in vivo*. The off-rate will be an important consideration for dosing experiments: if the expectation for a certain treatment is loss or decrease of mitophagy, the treatment window should be on the scale of weeks rather than days. This also means that increases in mitophagy will be easier to detect than decreases, and that detecting short term changes in mitophagic flux in tissues with high basal levels will be challenging. Going forward, it will be important to evaluate this parameter in different tissues, organisms, and metabolic conditions.

Many genes have been implicated in both ubiquitin-dependent and ubiquitin-independent mitophagy (12, 57, 58), however, these studies were primarily performed using cell culture systems with limited confirmation of conserved mechanisms *in vivo*. BNIP3, BNIP3L (Nix), and FUNDC1 have all been linked to hypoxia-induced mitophagy and HIF signaling (33). They contain domains to localize them to the mitochondrial outer membrane, and LIRs, which bind to LC3 and recruit the autophagosomal membrane (32). BNIP3 was found to mediate hypoxia-induced mitophagy in MEFs and murine lung tissue (8). In murine skeletal muscle, FoxO signaling is known to mediate fasting-induced autophagy via BNIP3, although neither mitophagy or hypoxia were analyzed (10). BNIP3 was also found to facilitate mitophagy in murine cortical neurons in a stroke model (59) and in murine hearts and HL1 cardiac muscle cells after myocardial ischemia/reperfusion injury (60). BNIP3L (NIX) has been linked to hypoxia-induced mitophagy in ischemic brain injury and heart ischemia/reperfusion injury in mice (61). FUNDC1 was shown to facilitate hypoxia-mediated mitophagy in HeLa cells (62, 63) and several murine tissues including platelets, liver, heart, and muscle (64) and also in cardiac ischemia/reperfusion injury (65). We disrupted each of these genes using CRISPR and found that only *bnip3* disruption prevented Hif-induced mitophagy in skeletal muscle. Importantly, disrupting *fundc1* and *bnip3la*

(*nix*) had no effect. Our results emphasize the importance of elucidating receptor-mediated mitophagy processes in a stress- and context-dependent manner *in vivo*.

There is conflicting evidence for how BNIP3 induces mitophagy. In MEFs, BNIP3 was shown to compete with Beclin-1 for binding to Bcl-2, allowing Beclin-1 to initiate autophagy (8). However, a separate study in MEFs and HEK293 cells, showed BNIP3 interacted with and stabilized PINK1, which recruited PARKIN to the mitochondrial outer membrane and initiated PINK1-PARKIN-dependent mitophagy (14). Indeed, pink1 was shown to be necessary for hypoxia-induced mitophagy in flies (13). However, we tested two mutant *pink1* alleles, *pink1* knockdown via antisense morpholino, and *prkn* disruption via CRISPR and found that none of these interventions prevented Hif-induced mitophagy in zebrafish muscle, indicating that *bnip3*-induced mitophagy is independent of the Pink1-Parkin ubiquitination system. In flies, *Pink1* mutation causes muscle degeneration (66–68), and BNIP3 overexpression can rescue the phenotype (14). In humans (69), monkeys (70), mice (38), and zebrafish (35) there is no evidence of direct muscle degeneration due to PINK1 mutation, indicating that there are important differences between vertebrate and invertebrate mitophagy mechanisms.

In summary, our study reveals fundamental piecemeal mitophagy dynamics during fasting and the molecular mechanisms of hypoxia-induced mitophagy, thereby providing a greater understanding of vertebrate muscle metabolism and *in vivo* mitochondrial quality control. Because there are few yeast homologs to vertebrate mitophagy receptors (71), higher-order model systems amenable to chemical and genetic screening such as zebrafish will be instrumental for uncovering novel and clinically impactful mitophagy regulatory mechanisms.

Limitations of Study

It is possible the dynamic extensions of $Lc3^+$ organelles we observe (Fig. 4*B* and Movie S3) are caused by Lc3 overexpression, and it will be important to explore these questions further using

knockin reporters expressed at endogenous levels. Improvements in zebrafish genome editing will make such inquiries feasible (72, 73).

ACKNOWLEDGEMENTS

Research was supported by NIH F32AA025271 and the American Liver Foundation (P.J.W.), NIH R37 NS083524 to J.W.H., and NIH R01DK090311, R01DK105198, R24OD017870 to W.G.. W.G. is a Pew Scholar in the Biomedical Sciences. We thank Tom Schwarz for helpful discussions. We thank Nadine Budrow for maintaining our zebrafish colonies. We thank Phil Elks for sharing *DA-hif* plasmids, Donghun Shin for sharing the p5E-2.8fabp10a plasmid, and Daniel Hesselson for sharing the *pink1*^{gi2} line. We thank the Harvard Medical School MicRoN team for access to microscopes and imaging expertise.

AUTHOR CONTRIBUTIONS

Conceptualization, P.J.W., J-M.H., J.W.H., and W.G.; Methodology, P.J.W., A.S., and J-M.H.; Investigation, P.J.W., E.D.Q., and K.A.L.; Writing – Original Draft, P.J.W. and W.G.; Writing – Review and Editing, P.J.W., A.S., J-M.H., E.D.Q., J.W.H. and W.G.; Supervision, J.W.H. and W.G.; Funding Acquisition, P.J.W., J.W.H., and W.G.

DECLARATION OF INTERESTS

J.W.H. is a founder and consultant to Caraway Therapeutics. W.G. is a consultant to Camp4 Therapeutics and receives royalties from FATE Therapeutics.

REFERENCES

1. Youle RJ (2019) Mitochondria—Striking a balance between host and endosymbiont. *Science* 365(6454).

2. Sandri M (2013) Protein breakdown in muscle wasting: Role of autophagy-lysosome and ubiquitin-proteasome. *Int J Biochem Cell Biol* 45(10):2121–2129.

3. Pickrell AM, Youle RJ (2015) The roles of PINK1, Parkin, and mitochondrial fidelity in parkinson's disease. *Neuron* 85(2):257–273.

4. Wrighton PJ, Oderberg IM, Goessling W (2019) There Is Something Fishy About Liver Cancer: Zebrafish Models of Hepatocellular Carcinoma. *Cell Mol Gastroenterol Hepatol* 8(3):347–363.

5. McWilliams TG, et al. (2016) Mito-QC illuminates mitophagy and mitochondrial architecture in vivo. *J Cell Biol* 214(3):333–345.

6. Yamashita SI, et al. (2016) Mitochondrial division occurs concurrently with autophagosome formation but independently of Drp1 during mitophagy. *J Cell Biol* 215(5):649–665.

7. Burman JL, et al. (2017) Mitochondrial fission facilitates the selective mitophagy of protein aggregates. *J Cell Biol* 216(10):3231–3247.

8. Zhang H, et al. (2008) Mitochondrial autophagy is an HIF-1-dependent adaptive metabolic response to hypoxia. *J Biol Chem* 283(16):10892–10903.

9. Sun N, et al. (2015) Measuring In Vivo Mitophagy. *Mol Cell* 60(4):685–696.

10. Mammucari C, et al. (2007) FoxO3 Controls Autophagy in Skeletal Muscle In Vivo. *Cell Metab* 6(6):458–471.

11. Pickles S, Vigié P, Youle RJ (2018) Mitophagy and Quality Control Mechanisms in Mitochondrial Maintenance. *Curr Biol* 28(4):R170–R185.

12. Harper JW, Ordureau A, Heo JM (2018) Building and decoding ubiquitin chains for mitophagy. *Nat Rev Mol Cell Biol* 19(2):93–108.

13. Kim YY, et al. (2019) Assessment of mitophagy in mt-Keima Drosophila revealed an essential role of the PINK1-Parkin pathway in mitophagy induction in vivo. *FASEB J*

33(9):9742–9751.

14. Zhang T, et al. (2016) BNIP3 protein suppresses PINK1 kinase proteolytic cleavage to promote mitophagy. *J Biol Chem* 291(41):21616–21629.

15. Lee JJ, et al. (2018) Basal mitophagy is widespread in Drosophila but minimally affected by loss of Pink1 or parkin. *J Cell Biol* 217(5):1613–1622.

16. Katayama H, Kogure T, Mizushima N, Yoshimori T, Miyawaki A (2011) A sensitive and quantitative technique for detecting autophagic events based on lysosomal delivery. *Chem Biol* 18(8):1042–1052.

17. Rojansky R, Cha MY, Chan DC (2016) Elimination of paternal mitochondria in mouse embryos occurs through autophagic degradation dependent on PARKIN and MUL1. *Elife* 5:e17896.

18. Cox AG, Goessling W (2015) The lure of zebrafish in liver research: Regulation of hepatic growth in development and regeneration. *Curr Opin Genet Dev* 32:153–161.

19. Kwan KM, et al. (2007) The Tol2kit: A multisite gateway-based construction Kit for Tol2 transposon transgenesis constructs. *Dev Dyn* 236(11):3088–3099.

20. Mosimann C, et al. (2011) Ubiquitous transgene expression and Cre-based recombination driven by the ubiquitin promoter in zebrafish. *Development* 138(1):169–177.

21. He C, Bartholomew CR, Zhou W, Klionsky DJ (2009) Assaying autophagic activity in transgenic GFP-Lc3 and GFP-Gabarap zebrafish embryos. *Autophagy* 5(4):520–526.

22. Sugiura A, McLelland G, Fon EA, McBride HM (2014) A new pathway for mitochondrial quality control: mitochondrial-derived vesicles. *EMBO J* 33(19):2142–2156.

23. Cadete VJJ, et al. (2016) Formation of mitochondrial-derived vesicles is an active and physiologically relevant mitochondrial quality control process in the cardiac system. *J*

Physiol 594(18):5343–5362.

24. Kaelin WG, McKnight SL (2013) Influence of metabolism on epigenetics and disease. *Cell* 153(1):56–69.

25. Elks PM, et al. (2013) Hypoxia Inducible Factor Signaling Modulates Susceptibility to Mycobacterial Infection via a Nitric Oxide Dependent Mechanism. *PLoS Pathog* 9(12):e1003789.

26. Ivan M, et al. (2001) HIFα targeted for VHL-mediated destruction by proline hydroxylation: Implications for O2 sensing. *Science* 292(5516):464–468.

27. Iliopoulos O, Levy AP, Jiang C, Kaelin WG, Goldberg MA (1996) Negative regulation of hypoxia-inducible genes by the von Hippel-Lindau protein. *Proc Natl Acad Sci* 93(20):10595–10599.

28. Harris JM, et al. (2013) Glucose metabolism impacts the spatiotemporal onset and magnitude of HSC induction in vivo. *Blood* 121(13):2483–2493.

29. Elks PM, et al. (2011) Activation of hypoxia-inducible factor-1α (hif-1α) delays inflammation resolution by reducing neutrophil apoptosis and reverse migration in a zebrafish inflammation model. *Blood* 118(3):712–722.

30. Berger J, Currie PD (2013) 503Unc, a Small and Muscle-Specific Zebrafish Promoter. *Genesis* 51(6):443–447.

31. Ronan B, et al. (2014) A highly potent and selective Vps34 inhibitor alters vesicle trafficking and autophagy. *Nat Chem Biol* 10(12):1013–1019.

32. Birgisdottir A, Lamark T, Johansen T (2013) The LIR motif – crucial for selective autophagy. *J Cell Sci* 126:3237–3247.

33. Yoo S-M, Jung Y-K (2018) A Molecular Approach to Mitophagy and Mitochondrial

Dynamics. *Mol Cells* 41(1):18–26.

34. Burger A, et al. (2016) Maximizing mutagenesis with solubilized CRISPR-Cas9 ribonucleoprotein complexes. *Development* 143(11):2025–2037.

35. Zhang Y, et al. (2017) Rescue of Pink1 Deficiency by Stress-Dependent Activation of Autophagy. *Cell Chem Biol* 24(4):471-480.e4.

36. Priyadarshini M, Tuimala J, Chen YC, Panula P (2013) A zebrafish model of PINK1 deficiency reveals key pathway dysfunction including HIF signaling. *Neurobiol Dis* 54:127–138.

37. Kaizuka T, et al. (2016) An autophagic flux probe that releases an internal control. *Mol Cell* 64(4):835–849.

38. McWilliams TG, et al. (2018) Basal Mitophagy Occurs Independently of PINK1 in Mouse Tissues of High Metabolic Demand. *Cell Metab* 27(2):439-449.e5.

39. An H, Harper J (2018) Systematic Analysis of Ribophagy in Human Cells Reveals Bystander Flux During Selective Autophagy. *Nat Cell Biol* 20(2):135–143.

40. An H, et al. (2019) TEX264 Is an Endoplasmic Reticulum-Resident ATG8-Interacting Protein Critical for ER Remodeling during Nutrient Stress. *Mol Cell* 74(5):891-908.e10.

41. Malide D, et al. (2016) A fluorescence-based imaging method to measure in vitro and in vivo mitophagy using mt-Keima. *Nat Protoc* 12(8):1576–1587.

42. Abudu YP, et al. (2019) NIPSNAP1 and NIPSNAP2 Act as “Eat Me” Signals for Mitophagy. *Dev Cell* 49(4):509-525.e12.

43. Fimia GM, et al. (2007) Ambra1 regulates autophagy and development of the nervous system. *Nature* 447(7148):1121–1125.

44. Skobo T, et al. (2014) Zebrafish ambra1a and ambra1b knockdown impairs skeletal muscle development. *PLoS One* 9(6):e99210.

45. Schweers RL, et al. (2007) NIX is required for programmed mitochondrial clearance during reticulocyte maturation. *Proc Natl Acad Sci* 104(49):19500–5.

46. Sandoval H, et al. (2009) Essential role for Nix in autophagic maturation of erythroid cells. *Nature* 454(7201):232–235.

47. Esteban-Martínez L, et al. (2017) Programmed mitophagy is essential for the glycolytic switch during cell differentiation. *EMBO J* 36(12):1688–1706.

48. Zhou Y, et al. (2019) Topology-dependent, bifurcated mitochondrial quality control under starvation. *Autophagy* Jul:1–13.

49. Abeliovich H, Zarei M, Rigbolt KTG, Youle RJ, Dengjel J (2013) Involvement of mitochondrial dynamics in the segregation of mitochondrial matrix proteins during stationary phase mitophagy. *Nat Commun* 4:2789.

50. Kolitsida P, et al. (2019) Phosphorylation of mitochondrial matrix proteins regulates their selective mitophagic degradation. *Proc Natl Acad Sci* 116(41):20517–20527.

51. Yang JY, Yang WY (2013) Bit-by-bit autophagic removal of parkin-labelled mitochondria. *Nat Commun* 4:2428.

52. Le Guerroué F, et al. (2017) Autophagosomal Content Profiling Reveals an LC3C-Dependent Piecemeal Mitophagy Pathway. *Mol Cell* 68(4):786-796.e6.

53. Romanello V, Sandri M (2013) Mitochondrial biogenesis and fragmentation as regulators of protein degradation in striated muscles. *J Mol Cell Cardiol* 55(1):64–72.

54. Friedman JR, Nunnari J (2014) Mitochondrial form and function. *Nature* 505(7483):335–343.

55. Rodríguez-Nuevo A, et al. (2018) Mitochondrial DNA and TLR9 drive muscle inflammation upon Opa1 deficiency. *EMBO J* 37(10):1–18.

56. Evans CS, Holzbaur EL (2020) Degradation of engulfed mitochondria is rate-limiting in Optineurin-mediated mitophagy in neurons. *Elife* 9:e50260.

57. Rodger CE, Mcwilliams TG, Ganley IG, Ganley IG (2018) Mammalian mitophagy – from in vitro molecules to in vivo models. *FEBS J* 285(7):1185–1202.

58. Anding AL, Baehrecke EH (2017) Cleaning house: Selective autophagy of organelles. *Dev Cell* 41(1):10–22.

59. Shi RY, et al. (2014) BNIP3 interacting with LC3 triggers excessive mitophagy in delayed neuronal death in stroke. *CNS Neurosci Ther* 20(12):1045–1055.

60. Hamacher-Brady A, et al. (2007) Response to myocardial ischemia/reperfusion injury involves Bnip3 and autophagy. *Cell Death Differ* 14(1):146–157.

61. Yuan Y, et al. (2017) BNIP3L/NIX-mediated mitophagy protects against ischemic brain injury independent of PARK2. *Autophagy* 13(10):1754–1766.

62. Liu L, et al. (2012) Mitochondrial outer-membrane protein FUNDC1 mediates hypoxia-induced mitophagy in mammalian cells. *Nat Cell Biol* 14(2):177–185.

63. Chen G, et al. (2014) A regulatory signaling loop comprising the PGAM5 phosphatase and CK2 controls receptor-mediated mitophagy. *Mol Cell* 54(3):362–77.

64. Zhang W, et al. (2016) Hypoxic mitophagy regulates mitochondrial quality and platelet activation and determines severity of I/R heart injury. *Elife* 5:e21407.

65. Zhou H, et al. (2017) Ripk3 induces mitochondrial apoptosis via inhibition of FUNDC1 mitophagy in cardiac IR injury. *Redox Biol* 13:498–507.

66. Clark IE, et al. (2006) Drosophila pink1 is required for mitochondrial function and interacts genetically with parkin. *Nature* 441(7097):1162–1166.

67. Yang Y, et al. (2006) Mitochondrial pathology and muscle and dopaminergic neuron degeneration caused by inactivation of Drosophila Pink1 is rescued by Parkin. *Proc Natl Acad Sci* 103(28):10793–10798.

68. Park J, et al. (2006) Mitochondrial dysfunction in Drosophila PINK1 mutants is complemented by parkin. *Nature* 441(7097):1157–1161.

69. Gasser T (2009) Mendelian forms of Parkinson's disease. *Biochim Biophys Acta - Mol Basis Dis* 1792(7):587–596.

70. Yang W, et al. (2019) CRISPR/Cas9-mediated PINK1 deletion leads to neurodegeneration in rhesus monkeys. *Cell Res* 29(4):334–336.

71. Mao K, Wang K, Zhao M, Xu T, Klionsky DJ (2011) Two MAPK-signaling pathways are required for mitophagy in Saccharomyces cerevisiae. *J Cell Biol* 193(4):755–767.

72. Hoshijima K, Jurynec MJ, Grunwald DJ (2016) Precise Editing of the Zebrafish Genome Made Simple and Efficient. *Dev Cell* 36(6):654–667.

73. DiNapoli SE, et al. (2020) Synthetic CRISPR/Cas9 reagents facilitate genome editing and homology directed repair. *Nucleic Acids Res* Epub. doi:10.1093/nar/gkaa085.

74. Mosimann C, Zon LI (2011) Advanced zebrafish transgenesis with Tol2 and application for Cre/lox recombination experiments. *Methods Cell Biol* 104:173–194.

75. Her GM, Chiang C-C, Chen W-Y, Wu J-L (2003) In vivo studies of liver-type fatty acid binding protein (L-FABP) gene expression in liver of transgenic zebrafish (Danio rerio). *FEBS Lett* 538(1–3):125–133.

76. Labun K, et al. (2019) CHOPCHOP v3: expanding the CRISPR web toolbox beyond

genome editing. *Nucleic Acids Res* 47(W1):W171–W174.

77. Choi TY, Ninov N, Stainier DYR, Shin D (2014) Extensive conversion of hepatic biliary epithelial cells to hepatocytes after near total loss of hepatocytes in zebrafish. *Gastroenterology* 146(3):776–788.

78. Don EK, et al. (2017) A Tol2 Gateway-Compatible Toolbox for the Study of the Nervous System and Neurodegenerative Disease. *Zebrafish* 14(1):69–72.

79. Priyadarshini M, Tuimala J, Chen YC, Panula P (2013) A zebrafish model of PINK1 deficiency reveals key pathway dysfunction including HIF signaling. *Neurobiol Dis* 54:127–138.

80. Cox AG, et al. (2016) Yap reprograms glutamine metabolism to increase nucleotide biosynthesis and enable liver growth. *Nat Cell Biol* 18(8):886–896.

SUPPORTING INFORMATION

Supporting information appendix includes methods, 4 figures, and 4 movies.

METHODS

Detailed methods are included in the online version of this paper.

Animal Studies: Zebrafish (*Danio rerio*) were maintained according to institutional animal care and use committee (IACUC-BIDMC #506-2015) protocols. Adult fish and larva were raised at 28.5 ^{o}C. All studies were performed in larval zebrafish before sex can be determined, and therefore sex was not taken into consideration. All embryos and larvae were raised and experimentally treated in E3 salt solution. For experiments involving larval feeding, embryos were provided live paramecia and larval AP-100 fish food (Zeigler) *ad libitum*.

Molecular Cloning and Transgenesis: Transgenic lines *Tg(ubi:mito-Keima,cryaa:Cerulean)*, *Tg(ubi:mito-GR)*, and *Tg(fabp10a:mito-GR)* were generated using *tol2* transgenesis (20, 74, 75). Plasmids generated or used are listed in the Key Resources Table. Middle entry vector pENTR:mito-Keima was generated via PCR using pHAGE mt-Keima IRES Puro as template and pENTR/D-TOPO kit (Invitrogen) following manufacturer's instructions. A Gateway reaction using LR Clonase II Plus (Invitrogen) generated the *Tg(ubi:mito-Keima,cryaa:Cerulean)* vector following manufacturer's instructions. Middle entry vector pME:mito-GR was generated using BP Gateway cloning using pCLBW cox8 EGFP mCherry (17) and pDONR221 (Invitrogen) using Gateway BP Clonase II Enzyme (Invitrogen) mix following manufacturer's instructions. LR Gateway cloning was used to generate *Tg(ubi:mito-GR)* and *Tg(-2.8fabp10a:mito-GR)*. Middle entry vector pENTR:DA-hif1ab(noStop) was generated using PCR to amplify DA-hif1ab minus the Stop codon from a plasmid containing DA-hif1ab (29), which was a gift from Phil Elks. An LR Gateway reaction generated the *Tg(-503unc45b:DA-hif1ab-2A-nlsEGFP,cryaa:mCherry)* vector

following manufacturer's instructions. *Tol2* mRNA was synthesized using mMessage mMachine SP6 *In vitro* Transcription kit (Invitrogen) following the manufacturer's instructions. To generate stable transgenic lines, 1-cell stage TU embryos were injected with the transgenesis vector and *tol2* transposase mRNA. Positive embryos were screened either for cyan fluorescent lenses (ubi:mito-Keima) or for EGFP fluorescence (ubi:mito-GR and fabp10a:mito-GR) and raised to adulthood. F0 adults were outcrossed to TL mates, the F1 generation clutches were screened for bright fluorescence, and potential founders were raised. Potential F1 founders were outcrossed again to TU or TL mates and screened for bright fluorescence and 1:1 ratio of WT to transgenic offspring indicative of single copy insertion (74). All experiments were performed on F2 or later generation larvae.

Hypoxia and Chemical Treatments: For MitoTracker analysis, larvae were exposed to 1 μM MitoTracker Green FM (Cell Signaling Technology) overnight in E3, washed in E3 twice, and prepared for imaging. For LysoTracker analysis, larvae were exposed to 1 μM LysoTracker Green DND-26 (Cell Signaling Technology) or LysoTracker Deep Red (Thermo Fisher Scientific) overnight in E3, washed in E3 twice, and prepared for imaging. For all drug treatment experiments, single clutches were used and split between experimental groups. If additional embryos were necessary, two clutches from sibling breeding pairs were combined and mixed to split randomly. For hypoxia experiments, E3 was reduced to approximately 1.7 mg/L O_2 by bubbling in a mixture of 95% N_2 and 5% O_2 for about 10 minutes. The larvae E3 in a 10 cm dish was replaced with about 40 mL of the hypoxic water, and the dish was moved to a hypoxia chamber, which was then flushed with the same mixture of 95% N_2 and 5% O_2 for about 10 minutes until an O_2 sensor (DO210, Extech Instruments) read 4.7%. The chamber was sealed and moved into the 28.5 ^{o}C incubator. For chemical hypoxia experiments, larvae were exposed to 60 μM or 100 μM DMOG (Tocris) or 10 μM FG-4592 (Cayman Chemical) in E3 from about 70 hpf to 98 hpf unless otherwise specified. For SAR405 experiments, larvae were split into cohorts

receiving vehicle (DMSO; Sigma Aldrich) or 100 μM DMOG and then those cohorts were split into cohorts receiving additional vehicle (DMSO) or 10 μM SAR405 (EMD Millipore).

Confocal Microscopy: Microscopy was performed using an inverted Ti2 (Nikon) microscope equipped with a Yokogawa CSUW1 spinning disc confocal unit, a CFI Apo LWD Lambda S 40XC WI (1.15 N.A.) objective lens (Nikon), and a Zyla 4.2+ sCMOS camera (ANDOR). Keima images were captured by exciting with 440 nm laser light and 561 laser light with ET Cy3/TRITC emission filter (Chroma) in triggered acquisition mode. Mito-GR images were captured using 488 nm laser light and 561 nm laser light with ET FITC/TRITC dual emission filter (Chroma) in triggered acquisition mode. For MitoTracker Green, LysoTracker Green, EGFP-Lc3, and nlsEGFP imaging, 488 nm excitation was utilized with a 525/36 FITC emission filter (Chroma). For Lysotraker Deep Red, a similar microscope equipped with a 640 nm laser and ET705/72m emission filter (Chroma) was utilized. For images involving both Keima and GFP signal, the EGFP images were uniformly frame-shifted (Nikon Elements) based on control images to account for the shift caused by using different dichroic mirrors. For the *in vivo* mitophagy dynamics time-lapse imaging (Fig. 3 and Movie 1), an iXon Life 888 EMCCD (ANDOR) was used for its increased light sensitivity and frame rate capacity, allowing greater time resolution. Larvae were anesthetized with 0.16 mg/mL Tricaine-S (Western Chemical, Inc.) and mounted on glass-bottom dishes (MatTek) in 0.8% low-melt point agarose in E3 containing Tricane. After the agar solidified, additional E3 + Tricane was added to keep the gel hydrated during imaging. For skeletal muscle imaging, the collection volume was centered on the ninth and tenth myotomes. For all quantitative experiments, images of all samples were collected with identical laser power, gain and exposure time.

Image Analysis: All mito-Keima image analysis was conducting using Imaris (Bitplane) software with either FIJI (ImageJ) or MATLAB (MathWorks) plugins to enable image mathematics. Raw images from Nikon Elements (.nd2) were converted to Imaris (.ims) file format using Imaris Image Converter (Bitplane) and imported to Imaris. A surface mask was drawn manually using

the Surfaces function to segment muscle tissue away from skin. A ratiometric image (FIJI or MATLAB) was generated by changing the data type to 32 Bit Float and applying the following equation: (Keima561 channel) / (Keima440 channel + 150). The 150 addition ensures that areas of low signal from both Keima561 and Keima440 were excluded. The ratiometric image normalizes for the decrease in signal intensity as imaging depth into the tissue increases and for small intensity differences between samples. Then, an isosurfaces thresholding algorithm was applied to the ratio channel, with 0.15 μm surface grain (smoothing) to eliminate noise, using a threshold value determined for each experiment from images of control fish. A size cutoff removed objects smaller than 2 voxels to eliminate additional noise. Obviously spurious surfaces were removed manually. Rarely, individual slices were removed from images to account for fish movement, which caused edge artifacts in some ratio images. Puncta density was determined by dividing the number of ratio surface objects by the total tissue surface volume. Mitophagy Index was determined by dividing the sum of all ratio surface object volumes by the total tissue surface volume. For mito-GR images, applying a deconvolution algorithm (Imaris) to adjust for the behavior of light of differing emission wavelengths (green and red) can reduce edge artifacts. Object tracking in time-lapse microscopy (Fig. 3 and Movie 1) was performed using Imaris software (Bitplane). Mitophagy surface masks were generated as above. Mitochondria surfaces were generated using a 0.325 μm surface grain (smoothing), background subtraction (diameter largest sphere = 1.219 μm), a manually determined florescence intensity threshold, and a size cutoff eliminating objects smaller than 15 voxels. Object tracking was performed on Ratio surface objects, using autoregressive motion, a maximum distance of 1.003 μm, a maximum gap size of 3 (without gap filling), and a track duration minimum of 5.534 s. We manually assessed each newly formed mitophagy isosurface object, defined as a $Ratio^{high}$ tracked object that was not present at time zero; other mitophagy puncta were considered stable. Using a combination of microscopy views, new objects were manually classified as new mitophagy, split mitolysosomes, or from

outside. For lysosome size analysis, LysoTracker Green z-stack images were acquired covering 8.8 μm depth within the skeletal muscle of the fish and analyzed using FIJI. First background subtraction using 50 μm rolling ball was performed, then a maximum intensity projection was generated, the area of muscle was isolated manually by drawing a gate, a threshold was automatically applied using the Triangle setting, touching objects were split using the watershed function, and objects were counted using the analyze particles function cutting off objects smaller than 2 pixels. The number and area of lysosomes were measured using the maximum intensity projection image, and the area of the drawn gate served as total tissue area.

Morpholino Injections: Morpholinos (GeneTools, LLC) were reconstituted to 1 mM in water, and about 2 nL was injected into the yolk of 1-cell stage embryos. The sequences are listed in the Reagents and Resources Table.

CRISPR: All CRISPR was performed using a variation of the high-efficiency protocol described (34). Guide RNA sequences were designed using CHOPCHOP (76) and chosen to target a 5' exonic region with the potential to introduce STOP codons in the event of frameshift. Alt-R crRNA (IDT) constructs were reconstituted and annealed with Alt-R tracrRNA (IDT) to form gRNA duplexes according to the manufacturer's instructions. Injection mixes were prepared by mixing 1 μL the gRNA duplex, 1 μL Duplex Buffer (IDT), and 1 μL ENGEN Spy Cas9 NLS (NEB) and allowing the mix to incubate at room temperature for at least 10 min. Approximately 2 nL of injection mix was injected into both the cell and yolk of 1-cell stage embryos. Efficient editing was confirmed by PCR and Sanger sequencing. For experiments using F0 CRISPR editing, the Sanger sequencing trace of each imaged larva was used to determine the extent of editing in a blinded manner. Editing was considered sufficient if trace files showed a mixture of multiple traces emerging near the PAM site. Images from larvae found to have low or no editing were removed from analysis. To generate the *pink1*^{ghm1} mutant allele, injected F0 embryos were raised and outcrossed to WT adults. A subset of each clutch was pooled, and genomic DNA was collected. The region surrounding the

PAM was PCR amplified and TOPO cloned, and at least 10 colonies were Sanger sequenced. Clutches containing suitable alleles (those resulting in early STOP codons) were raised to adulthood and outcrossed individually to find founder fish by tail-clipping and genotyping. The founder was identified to have a 76 bp deletion which also resulted in an early STOP codon, and this allele was bred into the ubi:mito-Keima line.

Genotyping: DNA from individual larvae was extracted using proteinase K (Invitrogen) and amplified by PCR with the primer pairs (IDT) listed in the Key Resources Table. The 5' primer of the *pink1*^{gi2} PCR genotyping primer pair was synthesized with a 5' 6-FAM (Fluorescein) fluorescent dye attachment necessary for DNA Fragment Analysis, in which small, fluorescently-labeled DNA fragments are electrophoretically separated such that precise changes in size (down to 1 bp) can be detected. The *pink1*^{gi2} mutant fish (35) were identified by a small deletion, which was detected using DNA Fragment Analysis (MGH CCIB DNA Core). The *pink1*^{ghm1} mutant fish were identified by a 76 bp deletion, described in the CRISPR section, which was detected by gel electrophoresis on a 2% agarose gel. Efficient editing in F0 high efficiency CRISPR experiments was confirmed by Sanger sequencing, as described in the CRISPR section.

QPCR: Three individual clutches of embryos were divided and treated with DMSO or 60 μM DMOG from 77 to 96 hpf, then homogenized in TRIzol reagent (ThermoFisher). RNA was isolated using chloroform extraction and isopropanol precipitation. First strand cDNA synthesis was performed using iScript Reverse Transcription Supermix for RT-qPCR kit (Invitrogen), and qPCR was performed on a CFX96 Real-Time System (Bio-Rad) using iTaq Universal SYBR Green Supermix (Bio-Rad), both according to the manufacturer's instructions. Primer sets were designed to have at least one exon-spanning primer and verified as efficient using a cDNA dilution series. For gene expression analysis, gene-of-interest threshold cycle (Ct) values were normalized to Ct values for the housekeeping gene *ef1a* and compared to the Ct values of the corresponding vehicle control using the ΔΔCt method.

Statistical Analyses: All graphs and statistical analyses were generated using Prism (GraphPad). All box and whisker plots display the median, 25th, and 75th percentile as the box and the minimum and maximum values as the whiskers. For comparisons between only two conditions, standard, unpaired, two-tailed Student's t-tests were employed, except for the qPCR experiment where paired tests were used. For comparisons within groups with 4 conditions, two-way ANOVA with Holm-Sidak's multiple comparisons test were employed. *P* values or an asterisk indicating significant differences as defined in the figure legends were included in each figure containing statistical analyses. Each dot represents an individual larva.

REAGENT or RESOURCE	SOURCE	IDENTIFIER
Experimental Models: Organisms/Strains		
Zebrafish: *Tg(CMV:EGFP-map1lc3b)zf155*	(21)	ZFIN ID: ZDB-GENO-091029-2
Zebrafish: *Tg(ubi:mito-Keima)*	This paper.	N/A
Zebrafish: *Tg(ubi:mito-GR)*	This paper.	N/A
Zebrafish: *Tg(fabp10a:mito-GR)*	This paper.	N/A
Recombinant DNA		
Plasmid: pHAGE mt-Keima IRES Puro	(16)	N/A
Plasmid: pENTR-mito-Keima	This paper.	N/A
Plasmid: pCLBW cox8 EGFP mCherry	(17)	Addgene Plasmid #78520
Plasmid: pENTR-mito-GR	This paper.	N/A
Plasmid: Gateway pDONR221	ThermoFisher	Cat#: 12536017
Plasmid: pENTR5'_ubi	(20)	Addgene Plasmid #27320
Plasmid: p5E-2.8fabp10a	(77)	Gift from Donghun Shin
Plasmid: p3E-2A-pCS2MCS-pA	(19)	Tol2 kit v2.0 plasmid #633
Plasmid: pDEST-tol2-cryaaCerulean	(19)	N/A

Plasmid: pDestTol2pA2	(19)	Tol2 kit v1.0 plasmid #394
Plasmid: pCS2_da-hif1ab	(29)	Gift from Phil Elks.
Plasmid: p5E_unc503	(30)	Addgene Plasmid #64020
Plasmid: p3E-2A-nlsEGFPpA	(19)	Tol2 kit v2.0 plasmid #459
Plasmid: p3E-MCS	(78)	Addgene Plasmid #75174
Plasmid: pDESTtol2pACrymCherry	(30)	Addgene Plasmid #64023
Plasmid: p5E-hsp70l	(19)	Tol2 kit v1.0 plasmid #222
Plasmid: pCS2FA-transposase	(19)	Tol2 kit v1.0 plasmid #396
Chemicals, Peptides, and Recombinant Proteins		
Dimethyl Sulfoxide (DMSO)	Sigma Aldrich	
DMOG	Tocris	Cat#: 4408
FG-4592	Cayman Chemical	Cat#: 15294
MitoTracker Green FM	Cell Signaling Technology	Cat#: 9074S
LysoTracker Green DND-26	Cell Signaling Technology	Cat#: 8783S
LysoTracker Deep Red	Thermo Fisher Scientific	Cat#: L12492
Tricane-S	Western Chemical (Thermo Fisher Scientific)	Cat#: NC0872873
Low Melting Point Agarose	Invitrogen (Thermo Fisher Scientific)	Cat#: 16-520-100

Engen Spy Cas9 NLS	New England Biolabs	Cat#: M0646M
LR Clonase II Plus enzyme	Invitrogen	Cat#: 12538120
Gateway BP Clonase II Enzyme mix	Invitrogen	Cat#: 11789020
Oligonucleotides		
Morpholino: Standard Control Oligo CCTCTTACCTCAGTTACAATTTATA	GeneTools, LLC	Standard Negative Control Oligo
Morpholino: *pink1* TCACAACCTACCCGTTCAAAGTCAG	(79)	GeneTools, LLC
Morpholino: *vhl* GGCATCGTCAAAGACAGGACAGTTC	(28)	GeneTools, LLC
Alt-R CRISPR-Cas9 crRNA: *pink1* TCTTCAGGTTGTCTGTCAGC	This paper.	IDT
Alt-R CRISPR-Cas9 crRNA: *bnip3* ATGCTCAGCACGAGTCGGGT	This paper.	IDT
Alt-R CRISPR-Cas9 crRNA: *bnip3la* (*nix*) CTGCTGGGGAACGGGAACCA	This paper.	IDT
Alt-R CRISPR-Cas9 crRNA: *fundc1* CAATGGTGGAGTCGAGTATT	This paper.	IDT
Alt-R CRISPR-Cas9 crRNA: *prkn* GTGCGGTTTAATTCCAGCCA	This paper.	IDT
Alt-R CRISPR-Cas9 crRNA: Non-targeting Control TGCTGATGTCTTGGTTGAAT	IDT	N/A
Alt-R CRISPR-Cas9 tracrRNA	IDT	Cat.#: 1072532

PCR Genotyping Primer Pair: *pink1 (gi2)* 5': /6-FAM/CGCTCACAGAGACCTCAAAT 3': GGGAAGGGTAAAGGAGTAGA	This paper.	IDT
PCR Genotyping Primer Pair: *pink1 (ghm1)* 5': CAGTAAAGCATGTTCTCAGCC 3': GTATCTCCTGACACAGAGCAG	This paper.	IDT
PCR Genotyping Primer Pair: *bnip3* 5': GTTCTTGGGTGGAGCTGCAT 3': TGTCACATGGTAGGCTTCCT	This paper.	IDT
PCR Genotyping Primer Pair: *bnip3la* (*nix*) 5': CTGGGTGGAGCTGGAGATGAAT 3': CTGTTGCAGGACGAGCTGCT	This paper.	IDT
PCR Genotyping Primer Pair: *fundc1* 5': GCAGAGAGTGAAGATGAATTG 3': AGCTTTCCAACTCTCTGAAA	This paper.	IDT
PCR Genotyping Primer Pair: *prkn* 5': GCTGTCTGAGGAGGTTTACC 3': CCCTGTGTCAGCATCAGAATTC	This paper.	IDT
qPCR Primer Pair: *ef1a* 5': GCGTCATCAAGAGCGTTGAG 3': TTGGAACGGTGTGATTGAGG	(80)	IDT
qPCR Primer Pair: *phd3* 5': CCGTCGTATGCTACAAGGTATGC 3': CTTCCTGTGAGATGGCTGTGAG	This paper.	IDT
qPCR Primer Pair: *hpxa*	This paper.	IDT

5': GCTCCACCGCAACATAAAGAGG 3': CCTTTACAGCGGTCAAGCTGAG		
qPCR Primer Pair: *pink1* 5': GAGCTGACTTTGAACGGGCAC 3': TCAGGATACTCCTCGCGAGC	This paper.	IDT
qPCR Primer Pair: *prkn* 5': TGTGGAGAAAAACGGTGGCT 3': ATCCGGCTCATTCGAACCAA	This paper.	IDT
qPCR Primer Pair: *bnip3la* (*nix*) 5': GTCCTGCAACAGTCCTCCAC 3': CCATACTGTCATCCTCTGACTG	This paper.	IDT
qPCR Primer Pair: *bnip3* 5': GCCTACCATGTGACAGTCCTAC 3': GTCTTCCTCTGACTGTGAGCTG	This paper.	IDT
qPCR Primer Pair: *fundc1* 5': GGCGAAGATGCAGAGAGTGAAG 3': CTGCAATGGGACCTGTGCTG	This paper.	IDT

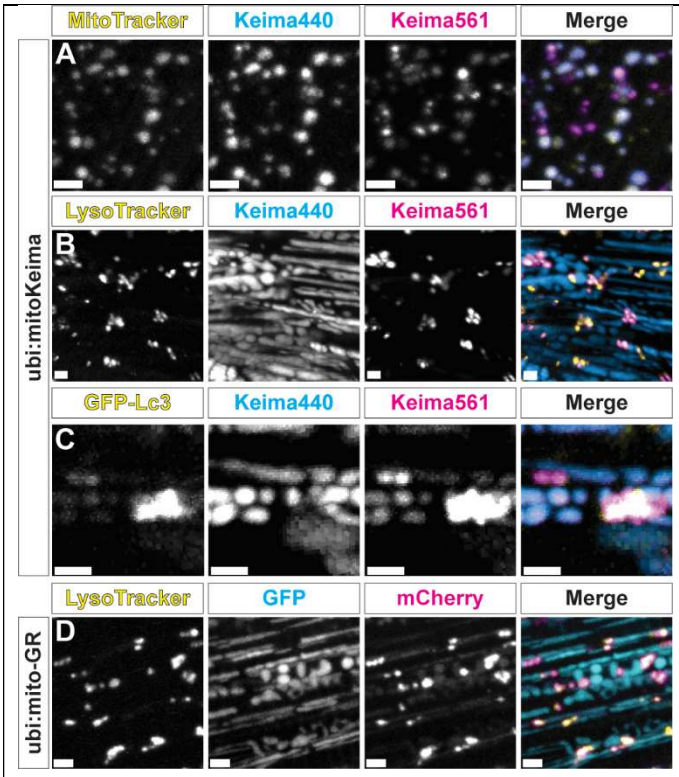

Fig. S1. Reporter zebrafish faithfully differentiates healthy mitochondria and those undergoing mitophagy. (*A*) Confocal 3D projection of skin cells of ubi:mito-Keima zebrafish larva treated with MitoTracker green showing colocalization of MitoTracker puncta with both Keima440 puncta and Keima561 puncta. (*B*) Confocal 3D projection of skeletal muscle cells of ubi:mito-Keima zebrafish larva treated with LysoTracker green showing colocalization between the Keima561 puncta and LysoTracker puncta. (*C*) Confocal 3D projection of a ubi:mito-Keima;CMV:GFP-Lc3 zebrafish larva demonstrating colocalization between Lc3 puncta and Keima561 puncta. (*D*) Confocal 3D projection of a ubi:mito-GR zebrafish larva treated with LysoTracker deep red demonstrating colocalization between LysoTracker and the $mCherry^{+}$;$EGFP^{-}$ puncta. Scale bars, 3 μm.

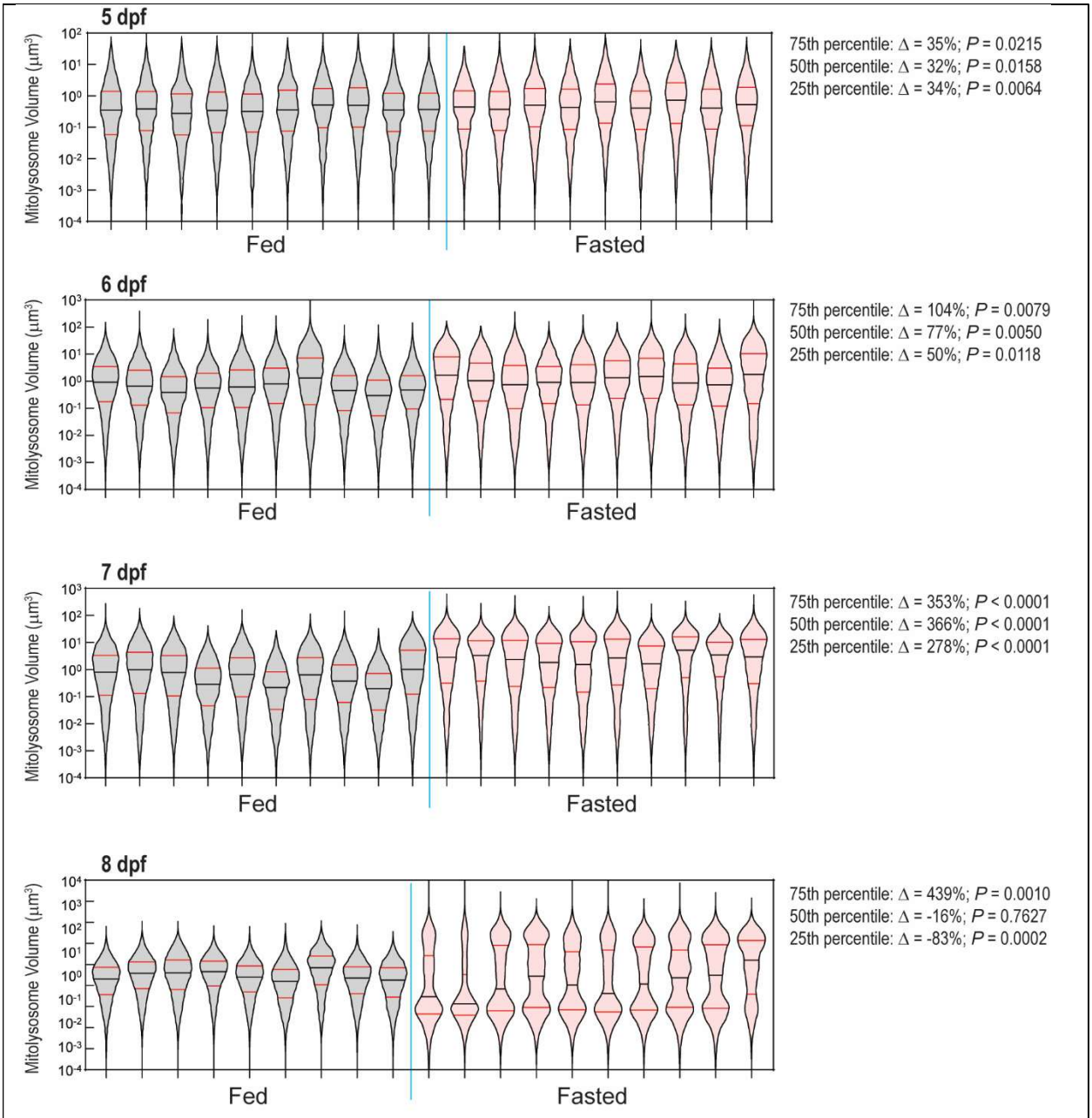

Fig. S2. Volumetric distribution analyses reveal early and late changes in mitolysosome dynamics during fasting. Violin plots of the mitophagy puncta volumes (μm^3) of individual fed and fasted fish depicted in Fig 2. A significant increase in the volume of the 25th, 50th, and 75th percentile mitolysosome is evident at 5 dpf and continues through 7 dpf. At 8 dpf, the fasted cohort displays a bimodal mitolysosome volume distribution indicative of an increase in both large and small mitolysosomes. Data shown are violin distribution plots. Black line is 50th percentile. Red lines are 25th and 75th percentiles. *P* is unpaired, two-tailed Student's t test comparing the indicated percentile in fasted and fed cohorts. Δ is the percentage change of the indicated percentile in each Fasted compared to Fed cohort.

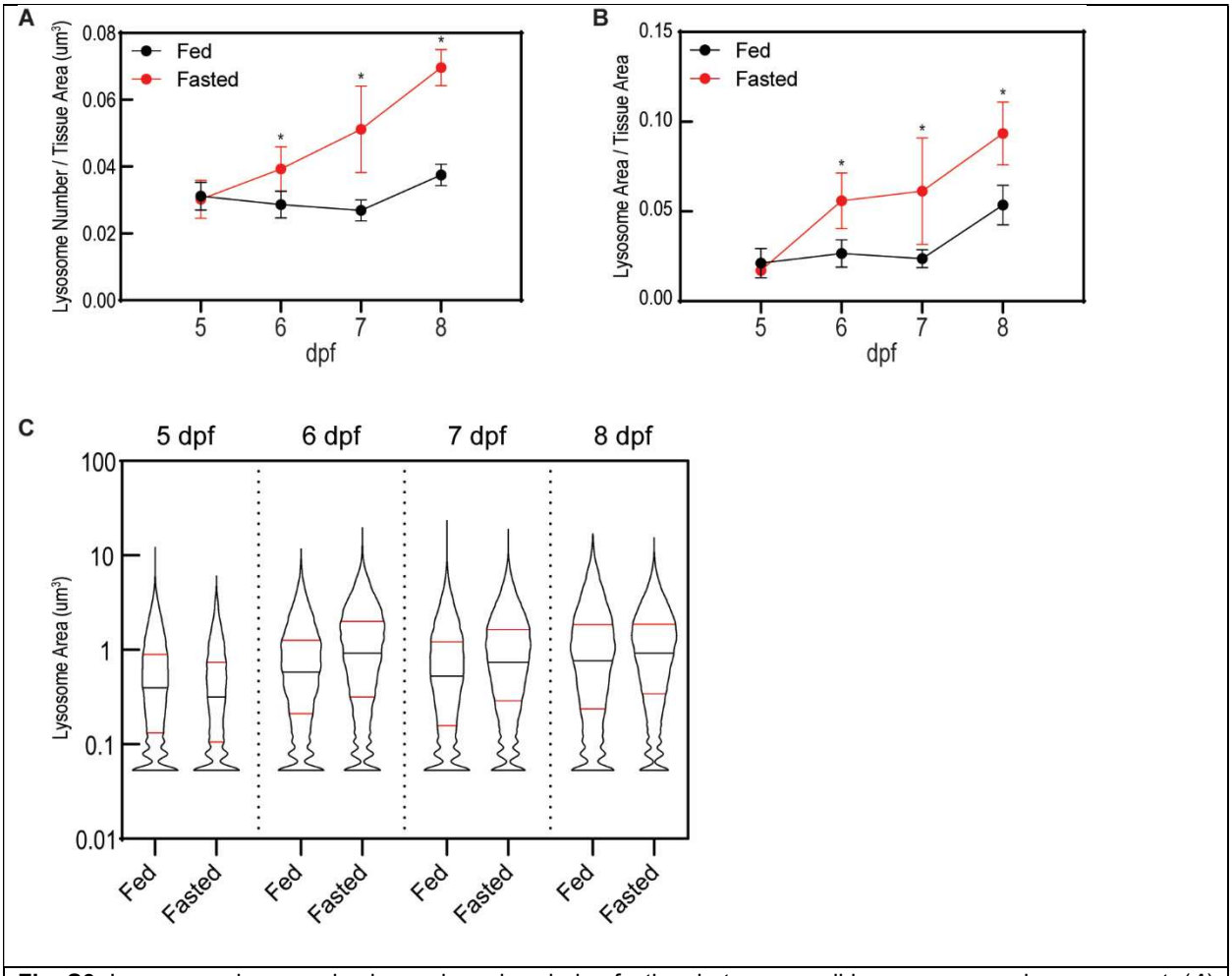

Fig. S3. Lysosomes increase in size and number during fasting, but very small lysosomes are always present. (*A*) Tracking the density of lysosomes in skeletal muscle in fed and fasted fish from 5 to 8 dpf. Data are the mean lysosome density calculated from at least 7 larvae. Bars show standard deviation, and * indicates $P<0.001$ (unpaired, two-tailed Student's t test) between the fed and fasted cohorts within each time point. (*B*) Tracking the total area of all lysosomes within the muscle. Data are the mean lysosome area per total tissue area calculated from at least 7 larvae—same larvae as (*A*). Bars show standard deviation, and * indicates $P<0.002$ (unpaired, two-tailed Student's t test) between the fed and fasted cohorts within each time point. (*C*) Violin plots demonstrating the area distribution of lysosomes in fed and fasted muscle from 5 to 8 dpf.

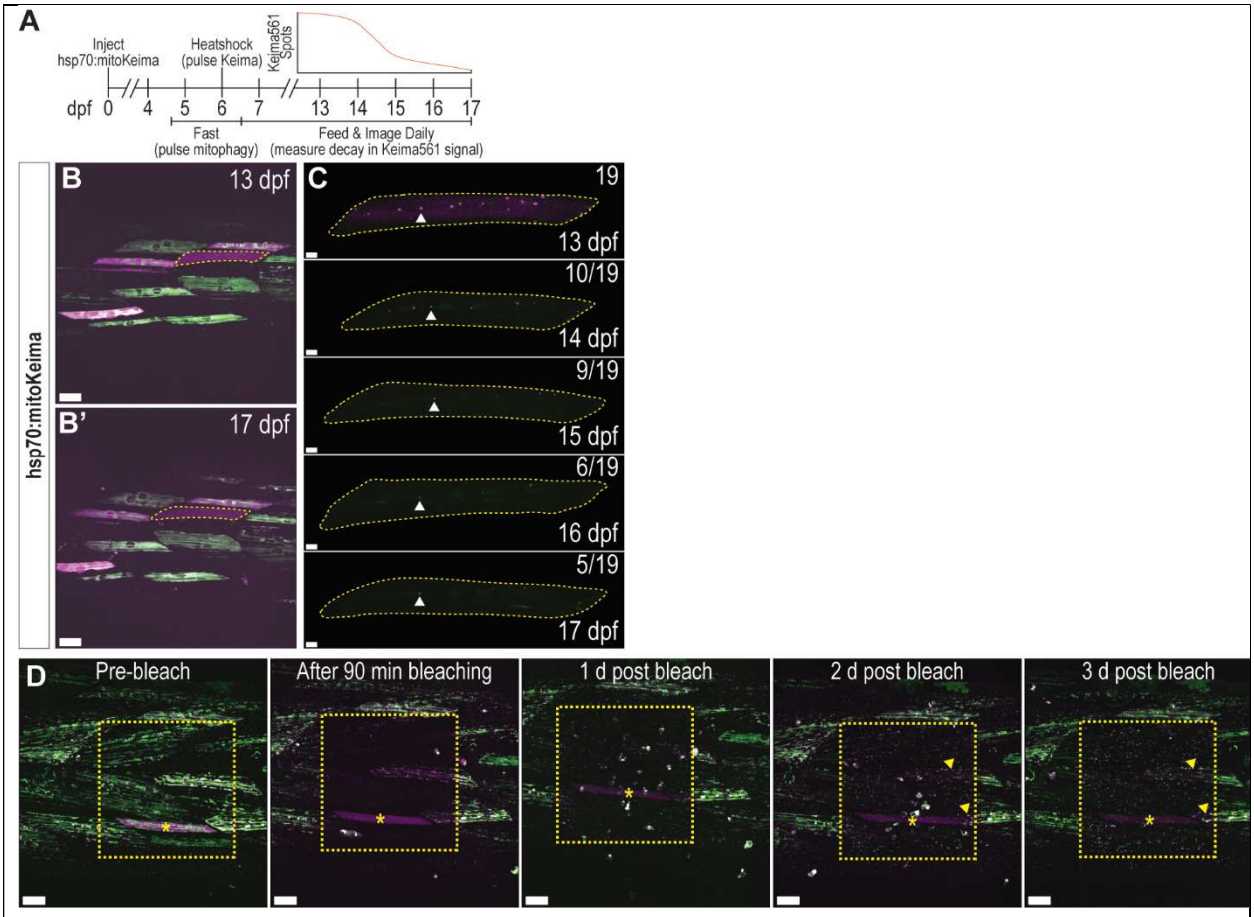

Fig. S4. Tracking individual mitophagy puncta over days. (*A*) Experimental design; similar experiment as Fig. 5. (*B,B'*) A cell from a second larva was imaged longitudinally from 13-17 dpf. Zoomed out images of the field of cells including the tracked cell (yellow dashed line). Scale, 30 μm. (*C*) Zoomed in images of the isolated tracked cell. The mitophagy puncta were quantified and displayed as the number in the top right corner of each panel. One mitophagy punctum (arrowhead) persists for the entire 4 days of imaging. Scale, 5 μm. (*D*) To demonstrate that the pulse of mito-Keima expression was transient and no new Keima protein was expressed, an area of muscle tissue was photobleached by exposure to high power 440 nm laser light for 90 minutes (yellow box), and the area was imaged longitudinally for 3 d post bleaching. Within the laser-exposed region one cell was completely bleached (*), and the signal does not return. Two other cells were partially bleached, and some mito-Keima signal recovers (arrow heads), presumably due to intracellular migration of labeled mitochondria.

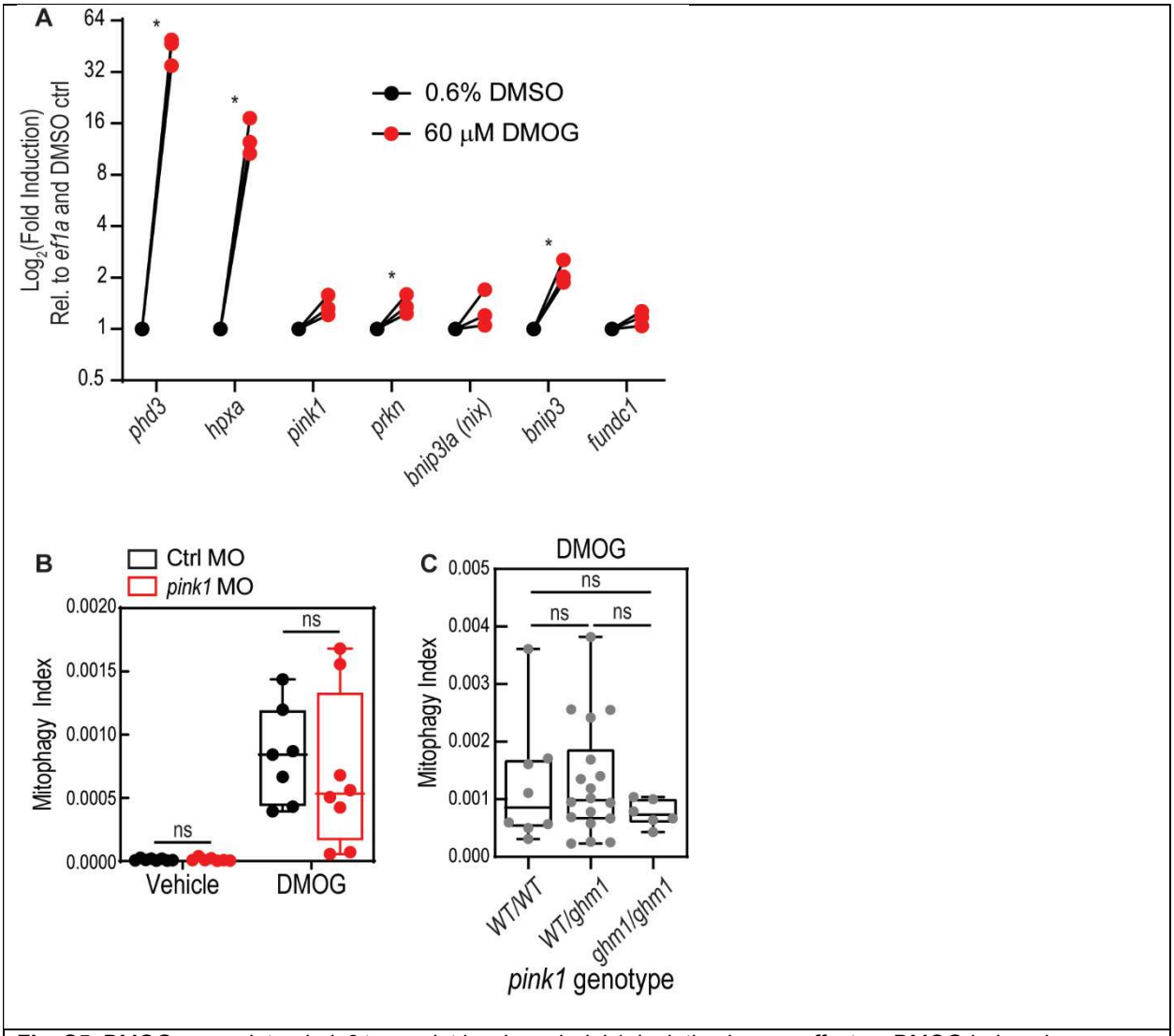

Fig. S5. DMOG upregulates *bnip3* transcript levels and *pink1* depletion has no effect on DMOG-induced mitophagy. (*A*) qPCR analysis of hif-target genes (*phd3* and *hpxa*) and mitophagy receptors (*pink1*, *prkn*, *bnip3la* (*nix*), *bnip3*, and *fundc1*. Connected points are transcript level data from pooled embryos from 3 individual clutches each split between DMSO control treatment (black) and DMOG treatment (red). **P*<0.05, two-tailed, ratio paired, Student's t test. (*B*) Mitophagy Index quantification of 72 hpf larvae injected with a control (Ctrl) MO or *pink1* MO and treated with vehicle control (DMSO) or DMOG from 48-72 hpf. Data shown are median, 1st and 3rd quartiles, minimum and maximum. ns, not significant (*P*>0.05, two-way ANOVA with Holm-Sidak's correction). Comparisons between all Vehicle and DMOG-treated samples were significant (*P*<0.05.). (*C*) Mitophagy Index quantification of 96 hpf larvae with the indicated *pink1* genotype treated with 100 μM DMOG from 72-96 hpf. Data shown are median, 1st and 3rd quartiles, minimum and maximum. ns, not significant (*P*>0.05, ordinary one-way ANOVA with Holm-Sidak's correction).